ISSN 0915-633X

NATIONAL INSTITUTE FOR FUSION SCIENCE

Interactions of Intermediate Energy Au Ions with Gases and Plasmas: Application to Plasma Diagnostics

M. Nishiura, H. Tawara, T. Ido, A. Shimizu, V.P. Shevelko
and LHD experimental group

(Received - Dec. 28, 2007)

NIFS-884 Jan. 2008

RESEARCH REPORT
NIFS Series

TOKI, JAPAN

Interactions of intermediate energy Au ions with gases and plasmas: Application to plasma diagnostics

M. Nishiura[1], H. Tawara[2], T. Ido[1], A. Shimizu[1], V.P. Shevelko[3] and LHD experimental group

[1] National Institute for Fusion Science, 322-6 Oroshi, Toki, Gifu, 509-5292 Japan

[2] Max Planck Institute for Nuclear Physics, Saupfercheckweg 1, D-69117 Heidelberg, Germany

[3] P.N. Lebedev Physical Institute, Leninskii prospect 53, 119991 Moscow, Russia

CONTENTS **Page**

Abstract.

The interactions of Au ions with gas and plasma targets are described in details with account for ionization, electron capture and stripping processes for application to heavy ion beam plasma probes (HIBP). A series of the theoretical cross sections for these processes are calculated and are applied to optimize the charge fractions of multi-charged Au (and also Cu) ions at the exit of the tandem accelerator at MeV energy range. In the charge changing processes, the theoretical charge fractions of multi-charged Au ions have been found to behave similarly as the experimental charge fractions under the neutral target areal density of ~ $1x10^{15}$ cm^{-2}. These cross sections are also used for estimating the attenuation of MeV energy ion beams in core and edge plasmas of the Large Helical Device (LHD). The signal levels of Au^{+} and Au^{2+}, which are detected at the primary beam monitor and the energy analyzer, are discussed quantitatively. These results give us some confidence to the enhanced availability of the HIBP system, leading to high precision diagnostics for plasma potentials, their fluctuations, and densities in a thermo-nuclear plasma.

Keywords: cross sections, tandem accelerator, charge changing process, negative ions, multi-charged ions, heavy ions, plasma diagnostics

1. Introduction

In high-temperature thermo-nuclear fusion plasmas, their electrostatic potential and density fluctuations are believed to be the major factors which strongly influence the plasma confinement properties and stabilities and, thus, it is critically important to know the detailed variations (in time and location) of such parameters inside plasmas. A heavy ion beam probe (HIBP) system is one of the effective diagnostic techniques to measure simultaneously the plasma electrostatic potential, its fluctuations and density fluctuations at a particular plasma location. The HIBP system of the Large Helical Device (LHD) was designed [1], and has been developed to measure LHD plasma potential distributions using the energy-analyzed ion beam passing through plasmas [2]. For the LHD-HIBP system, the negative gold ions (Au^{-}) are injected into a gas target in a tandem accelerator with 3 MV terminal voltage where a part of negative gold ions is converted into Au^{+} beam [3]. Then, after further acceleration up to 6 MeV, Au^{+} ions are injected into the main LHD plasmas collisions with plasma particles, Au^{+} ions are

ionized into Au^{2+} ions which come out from the plasma. By measuring the variation of energy and intensities of Au^{2+} ions, one can estimate the plasma potential, plasma density and their variations at a particular location inside the plasmas which the ions collide with. Typical LHD plasma parameters are: the electron density $N_e \sim 10^{13}$ - 10^{14} cm^{-3}, electron temperature at the plasma edge $T_e^{edge} \sim$ 1 - 100 eV and in the plasma core $T_e^{core} \sim 10$ keV.

In the present paper, in order to investigate interactions of Au ions with gas and plasma targets, basic data such as ionization, electron-capture and stripping cross sections are calculated in various gases over a wide range of ion energy. Besides, to know their transmission rates through plasmas, recombination rate coefficients of Au^{+} and Au^{2+} ions with plasma electrons are also calculated for the plasma electrons with Maxwellian velocity distributions at temperatures T_e = 1 eV – 10 keV. Furthermore, for comparison, some similar cross sections are also calculated for Cu ions as another possible candidate for HIBP system.

As we are interested maily in behavior of the projectile ions, following atomic processes are considered:

1. Ionization of a projectile X^{q+} by a target atom A:

$$X^{q+} + A \rightarrow X^{(q+m)+} + me + \Sigma A\,, \qquad (1)$$

where q denotes the charge of the projectile ion X^{q+} including a negative ion (q = -1) and a neutral atom (q = 0), A the target atom, m the number of ejected electrons, and sum ΣA means all possible states of the target after collision including ionization and excitation processes. Single ionization (SI) corresponds to m =1, and multiple ionization (MI) to m > 1. Sometimes, projectile ionization (1) is also called *electron loss* or *electron stripping*, since additional free electrons are involved after collisions.

2. Electron capture (EC) by a projectile:

$$X^{q+} + A \rightarrow X^{(q-1)+} + A^{+} \qquad (2)$$

The reaction (2) is also called *charge-exchange* or *charge-transfer*.

3. Ionization of a projectile via electron capture by a target (IEC):

$$X^{q+} + A^{a+} \rightarrow X^{(q+1)+} + A^{(a-1)+} \qquad (3)$$

The target A^{a+} can be a neutral atom (a = 0) or an ion (a ≥ 1). The reaction (3) is the projectile ionization through capture of a projectile electron by the target which is an important ionization process, particularly in high temperature plasmas, and should be considered along with ionization, eq. (1).

4. Photorecombination (PR) of a free electron:

$$X^{q+} + e \rightarrow X^{(q-1)+} + \hbar\omega \,, \qquad (4)$$

where $\hbar\omega$ represents a photon emitted. Capture of a free electron can occur via other processes (see section 6).

A list of the calculated cross sections and rates for different processes involving Au ions is given in Table 1 together with energy and temperature range, methods and codes used. Similar cross sections were also calculated for Cu ions as an alternative candidate for the LHD-HIBP system. Detailed description of the methods and codes used for the present calculations are given in the following sections.

Table 1. List of calculated cross sections and rates for atomic processes involving projectile Au and Cu ions.

Process, equation	**Calculated value**	**Projectile**	**Target**	**Energy, MeV**	**Method, code**
SI and MI (1)	cross sections	Au^-, Au^{q+}, $0 \le q \le 2$	H, He, Ar, Xe	0.05 - 10	Firsov model [3]
SI and MI (1)	cross sections	Cu^-, Cu^{q+}, $0 \le q \le 2$	Ar	0.05 - 10	Firsov model [3]
SI (1)	cross sections	Au^+, Au^{2+}	e, H^+, H, He, He^+, He^{2+}	0.1 - 50	LOSS code [4]
SI (1)	cross sections	Au^+	C^{q+} $0 \le q \le 6$	0.3 - 50	LOSS code [4]
EC (2)	cross sections	Au^{q+} $0 \le q \le 4$	H, He, Ar	0.1 - 100	CAPTURE code [5]
EC (2)	cross sections	Cu^{q+} $0 \le q \le 4$	Ar	0.1 - 100	CAPTURE code [5]
EC (2)	cross sections	Au^+, Au^{2+}	H, H_2, He, He^+	0.1 - 100	CAPTURE code [5]

EC (2)	cross sections	Au^{q+} $0 \le q \le 4$	Ar, Xe	0.1 - 10	CAPTURE code [5]
EC (2)	cross sections	Cu^{q+} $0 \le q \le 5$	Ar	0.1 - 20	CAPTURE code [5]
IEC (3)	cross sections	Au^{+}, Au^{2+}	H^{+}, He^{+}, He^{2+}	0.1 – 200	CAPTURE code [5]
PR (4)	cross sections	Au^{+}	*e*	0.1 - 10	formula [6]
PR (4)	rate coefficients	Au^{+}, Au^{2+}	*e*	T_e = 0.3 eV – 10 keV	formula [6]

2. Atom-atom interaction potential

For solving many problems in atomic and plasma physics, *e.g.*, to determine elastic scattering cross sections, stopping power, energy straggling, energy transfer, distance of closest approach between two colliding particles, *etc*., one has to use a proper atom-atom (or ion-atom) interaction potential V(r) given as a function of the inter-nuclear separation r. A survey of how to construct such a potential using two charge densities of each colliding atomic particle is given in [4]. Authors analyzed the potentials V(r) calculated for a number of atom-atom collision systems and found a scaling potential which provides the best fit to all calculated ones in a universal form (the so-called *Biersack-Ziegler universal potential*):

$$V(r) = \frac{Z_1 Z_2 e^2}{R} \phi(r/a) \tag{5}$$

with the screening function $\phi(x)$ given by

$$\phi(x) = 0.1818 \cdot \exp(-3.2x) + 0.5099 \cdot \exp(-0.9423x) + \\ + 0.2802 \cdot \exp(-0.4028x) + 0.02817 \cdot \exp(-0.2016x), \quad x = r/a \tag{6}$$

where Z_1 and Z_2 denote the nuclear charges of the colliding particles, respectively, e the electron charge, and a constant depending upon the colliding particles given as follows:

$$a = 0.8854/(Z_1^{0.23} + Z_2^{0.23}) \ , \tag{7}$$

if r is in the atomic units of a_0 ($a_0 = 0.529 \cdot 10^{-8}$ cm = 0.529 Å), or

$$a = 0.8854 \cdot 0.529 / (Z_1^{0.23} + Z_2^{0.23}) \quad , \tag{8}$$

if r is in Å. If V(r) is in eV and r in Å, then V(r) should be multiplied by 14.42 eV ·Å.

Figure 1 displays examples of the interatomic potentials V(r) calculated using eqs. (5), (6), and (8) for Au-Ar as well as for Kr-C colliding systems in comparison with that in a free-electron model [5].

Let us now estimate the scattering cross section which can be lost in the experimental setup due to its limited geometry. In our setup, the largest scattering angle acceptable in the laboratory system with the radius of a diaphragm of gas target, the radius (half-width) of the Faraday cup, and the length of the gas cell being as 5.0, 7.5, and 706 mm, respectively, is given by:

$$\Theta_{\max}^{setup} = \arctan\left(\frac{12.5}{706}\right) = \arctan 0.0177 = 0.0177\, rad \quad . \tag{9}$$

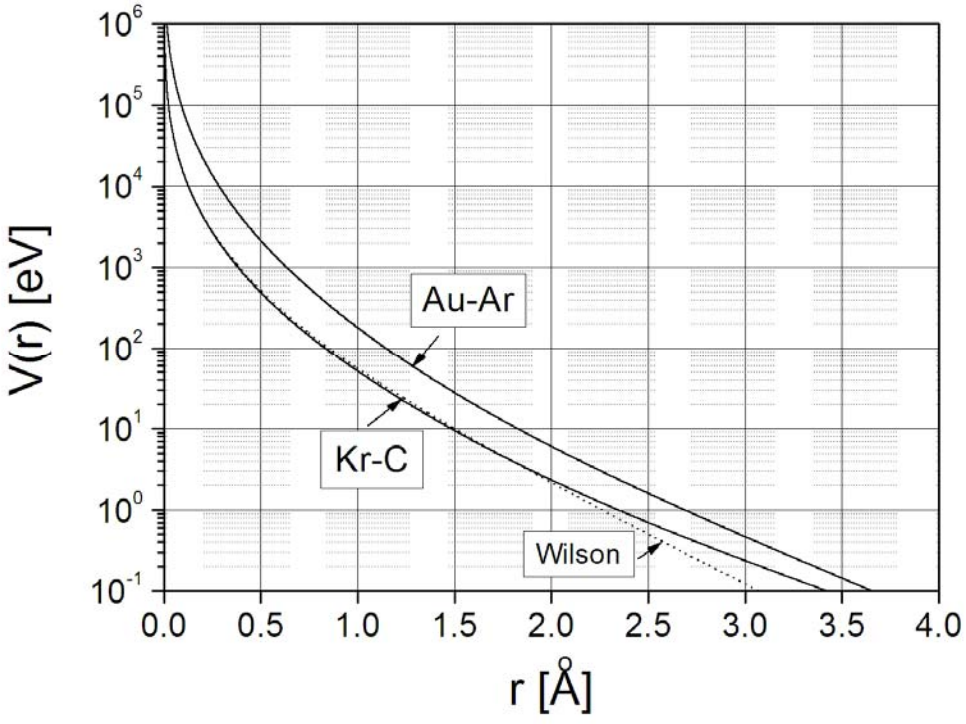

Fig. 1. Calculated interatomic potentials for Au-Ar and Kr-C systems, eqs. (5), (6), and (8), as a function of the inter-nuclear distance r. Dotted curve corresponds to a calculated potential for Kr-C interaction in a free-electron model [5].

Then the total maximum angle which can be use for observations is (in the center-of-mass (c.m.) system):

$$\Theta_{\max}^{tot} = \Theta_{\max}^{setup} + \arcsin\left(\frac{M_P}{M_T}\sin\Theta_{\max}\right) = 0.0177 + \arcsin\left(0.0177 \cdot \frac{197}{39.94}\right) = 0.105\ rad. \quad (10)$$

where M_P and M_T are the masses of projectile and target atoms, respectively. Taking into account the dependence between the scattering angle and the impact parameter b in the c.m. system, it is possible to find the minimum impact parameter $b_{\min}$ which can be detected in our setup. One can use the following relation between the scattering angle and impact parameter given in [6]

$$\Theta = \pi - 2b\int_{r_0}^{\infty} \frac{dr}{r^2\left[1 - V(r)/E_c - b^2/r^2\right]^{1/2}} \quad (11)$$

where E_c is the c.m. energy of the system, and r_0 is the distance of the closest approach which is found from the following equation:

$$1 - V(r_0)/E_c - b^2/r_0^2 = 0\,. \quad (12)$$

Equation (11) can be represented in other forms suitable for integration. Using the scaling parameters

$$x = r/a,\ p = b/a,\ \varepsilon = E_c/(Z_1 Z_2 e^2/a)\,, \quad (13)$$

then one has

$$\Theta = \pi - 2\int_{x_0}^{\infty} \frac{p\,dx}{x^2\left[1 - \Phi(x)/(x\varepsilon) - p^2/x^2\right]^{1/2}} \quad (14)$$

where

$$1 - \Phi(x_0)/(\varepsilon x_0) - p^2/x_0^2 = 0\,. \quad (15)$$

One can also use a 'trigonometric' form with a substitution $x = x_0/\cos\theta$ in eq. (14) (see [7]):

$$\Theta = \pi - \frac{2p}{x_0}\int_0^{\pi/2} \frac{\sin\theta\, d\theta}{\left[1 - \dfrac{\Phi(x_0/\cos\theta)}{(x_0/\cos\theta)\,\varepsilon} - \left(\dfrac{p^2}{x^2}\right)\cos\theta\right]^{1/2}}\,. \quad (16)$$

At $\theta = \pi / 2$, the integrand in eq. (16) is equal to unity.

In the case of Au^+ ions with the energy of E_p = 3 MeV incident on Ar atoms, one has

$$E_c = \frac{M_T}{M_T + M_P} E_P = 506330 \;\; eV, \;\; a \;\; = 0.100, \;\; \varepsilon = 2.47 \;\; , \qquad (17)$$

where a is defined in eq. (8). Using eqs. (5) - (6) for Au-Ar potential with Z_1=79 and Z_2=18, and solving eq. (12), one get the minimum impact parameter of

$$b_{min} = 0.2 \text{ Å}. \qquad (18)$$

This means that all particles under collisions with impact parameters $b < b_{min}$ are scattered away and can not be detected by our detector setup, and the corresponding scattering cross section at Au projectile energy of 3 MeV can be estimated as

$$\pi \, b_{min}^2 = 1.3 \text{ x } 10^{-17} \text{ cm}^2. \qquad (19)$$

Below we will see that this is small compared to ionization and electron capture cross sections which are of the order of $10^{-16} – 10^{-15}$ cm^2 in our conditions. Thus, it is believed that, in principle, no experimental geometries should influence comparison between the present calculations and observation.

3. Ionization of Au ions in collisions with gases at low energies. The Firsov model

Theoretical treatments of collision processes of atom-atom collisions at relatively low energies (relative velocity v = 5 x $10^6 – 10^8$ cm/s ~ 0.02 – 0.5 a.u., 1 a.u. of velocity corresponds to ~ 2.2 x 10^8 cm/s, which corresponds to the kinetic energy of ~ 25 keV/u) are quite complicated due to formation of so-called quasi-molecules which play a critical role. Therefore, only limited theoretical as well as experimental investigations have been reported so far. Among them, Firsov [7] treated them and developed relatively simple formulations for calculating the many-electron ionization (often called differently such as stripping, loss or detachment particularly for negative ions) cross sections of the projectile, eq. (1), applicable up to ionization of m = 4 electrons. The model is based on the classical treatment provided that the distance between neighboring energy levels of a quasi-united system of colliding atoms is smaller than the energy transferred to the projectile during collisions. The model uses the Thomas-Fermi potential for interactions between two colliding atoms with nuclear charges, Z_1 and Z_2, and has the following expression for ionization cross section [7]:

$$\sigma(\mathrm{v}) = 3.3\times10^{-15}\ cm^2\ \left(Z_1+Z_2\right)^{-2/3}\left[\left(\left(Z_1+Z_2\right)^{5/3}\times 4.3\times10^{-8}\,\mathrm{v}/I_m\right)^{1/5}-1\right]^2 \quad (20)$$

where v is the relative velocity in cm/s and I_{m} is the total ionization energy (in eV) required for removing m outmost electrons:

$$I_m = \sum_{q=q_i}^{m-1+q_i} I_{q,q+1} \quad . \quad (21)$$

Here $I_{q,q+1}$ is the single ionization energy from the charge q to q+1; for negative ions, summation on q starts from q_i = -1. For example, the total minimal energy I_4 required for the ionization of four electrons in Au^- ion is estimated to be:

$I_4 = I_{-1,3} = I_{-1,0}(Au^-) + I_{0,1}(Au^0) + I_{1,2}(Au^+) + I_{2,3}(Au^{2+})$
$= 2.28 + 9.23 + 20.5 + 37.4 = 69.4$ eV.

Introducing the scaled cross section and velocity parameters

$$\sigma_0 = \left[3.3\times10^{-15}/\left(Z_1+Z_2\right)^{2/3}\right] cm^2,\ \ u_0 = \left[23\times10^6\ I_m/\left(Z_1+Z_2\right)^{5/3}\right] cm/s\,, \quad (22)$$

eq. (20) can be written in the following closed form:

$$\sigma/\sigma_0 = \left[\left(\mathrm{v}/u_0\right)^{1/5}-1\right]^2 \quad . \quad (23)$$

This dependence in eq. (23) is reproduced in Fig. 2. Using eq. (23) and knowing a relative velocity of colliding particles v and the energy I_{m} required for removing m electrons, one can get the ionization cross sections at relatively low energies. The model can be applied for slow collisions (v < 1 a.u.) between heavy ions in low charge states with ejection up to four electrons (m ≤ 4). The uncertainty of the Firsov model is about a factor of 2.

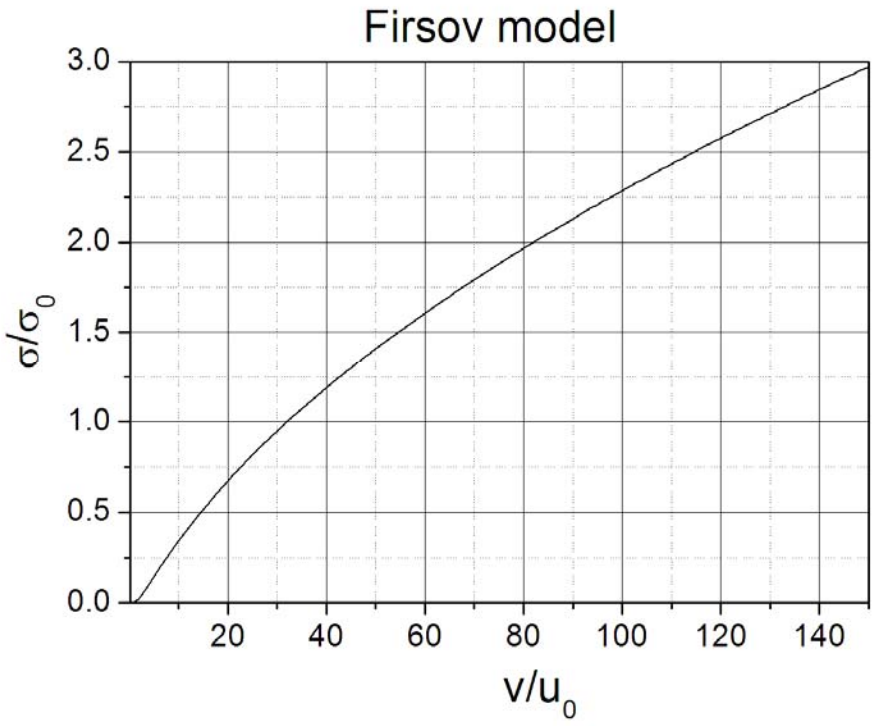

Fig. 2. Firsov universal curve to calculate ionization cross sections at low collision energies based upon eq. (23). The scaling parameters σ_0 and u_0 are given in eq. (22).

Single- and multiple-electron ionization cross sections calculated by the Firsov model for 3 MeV Au and Cu ions colliding with H and various noble-gas atoms are given in Table 2 and Fig. 3. It is interesting to note that the ionization cross sections, defined by eqs. (22) - (23), do not change very much and are nearly independent (within 10 - 15 %) of the target atoms because the Au projectiles are heavier than any target considered here. These data (together with electron capture cross sections) will be used in section 5 for estimation of charge-state fraction distributions of ions created in collisions of negative Au^- and Cu^- ions with gaseous targets.

Table 2. Single- and multiple-ionization cross sections (10^{-16} cm^2) for Au and Cu ions colliding with different gases at energy of E = 3 MeV, based upon the Firsov model, eqs. (22) - (23).

	Au + H	**Au + He**	**Au + Ar**	**Au + Xe**	**Cu + Ar**
$\sigma_{-1,0}$	34.8	34.9	35.8	39.4	59.8
$\sigma_{-1,1}$	15.2	15.3	15.9	16.9	21.9
$\sigma_{-1,2}$	8.6	8.63	9.1	9.9	11.3
$\sigma_{-1,3}$	5.4	5.42	5.8	6.42	6.9
$\sigma_{0,1}$	17.1	17.2	17.8	18.9	23.7
$\sigma_{0,2}$	9.0	9.01	9.5	10.3	11.6

$\sigma_{0,3}$	5.5	5.54	5.9	6.5	6.9
$\sigma_{0,4}$	3.44	3.46	3.8	4.3	4.6
$\sigma_{1,2}$	11.1	11.1	11.7	12.6	14.0
$\sigma_{1,3}$	6.05	6.07	6.5	7.13	7.5
$\sigma_{1,4}$	3.96	3.98	4.3	4.85	4.8
$\sigma_{2,3}$	7.9	7.9	8.3	9.1	9.9
$\sigma_{2,4}$	4.53	4.55	4.9	5.47	5.52
$\sigma_{2,5}$	3.1	3.1	3.37	3.86	3.6
$\sigma_{3,4}$	6.3	6.3	6.7	7.4	4.2
$\sigma_{3,5}$	3.7	3.7	4.0	4.54	59.8
$\sigma_{4,5}$	5.32	5.35	5.7	6.35	6.1
$\sigma_{4,6}$	3.12	3.14	3.4	3.91	3.4

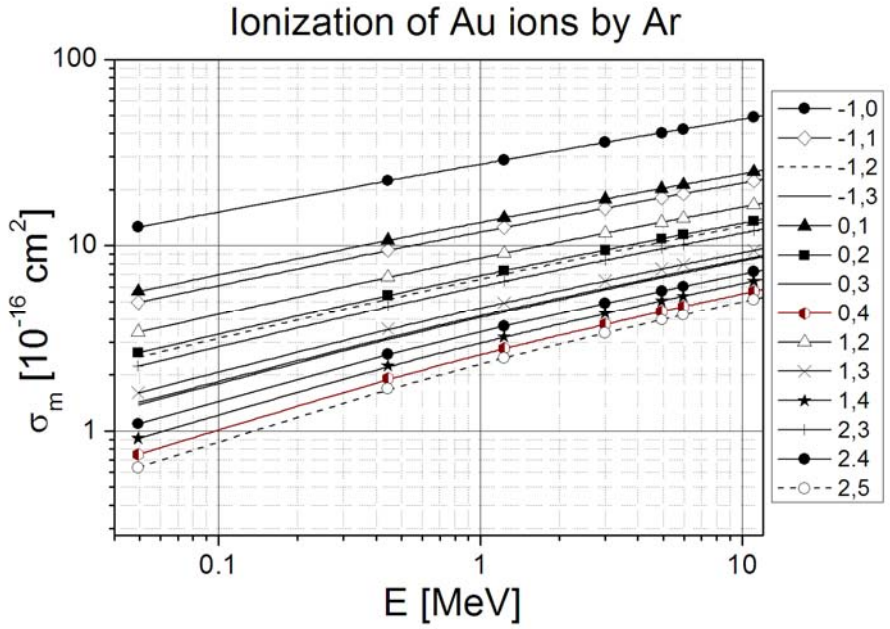

Fig. 3. Calculated single and multiple ionization cross sections of Au ions by Ar impact using the Firsov model, eqs. (22) - (23). Notations of ion charge before and after collision *q, q*+ *m* are given in the right-hand side of the figure, *e.g.,* -1,1 means double ionization of Au^- ions.

Table 3. The total ionization energies $I_{q,q+m}$ (in eV) for Au and Cu ions taken from [8]). q is the initial ion charge and m denotes the number of electrons to be ejected.

Au ions				**Cu ions**			
q, $q+m$	$I_{q,q+m}$ (eV)	q, $q+m$	$I_{q,q+m}$ (eV)	q, $q+m$	$I_{q,q+m}$ (eV)	q, $q+m$	$I_{q,q+m}$ (eV)
-1,0	2.28	1,2	20.5	-1,0	1.24	1,2	20.29
-1,1	11.52	1,3	57.9	-1,1	8.97	1,3	57.1
-1,2	32.12	1,4	112.1	-1,2	29.3	1,4	112.0
-1,3	69.49	2,3	37.4	-1,3	66.1	2,3	36.83
0,1	9.23	2,4	91.6	0,1	7.73	2,4	92.0
0,2	29.83	2,5	162.6	0,2	28.0	2,5	172.0
0,3	67.23	3,4	54.2	0,3	64.8	3,4	55.2
0,4	138.2	3,5	125.2	0,4	120.0	3,5	135.0
		4,5	71.0			4,5	79.9
		4,6	158.8			4,6	183.0

It is interesting to compare the Firsov model calculations with experimental data for ionization of negative ions by neutrals at low collision energies. There are several data on single ($\sigma_{-1,0}$), double ($\sigma_{-1,1}$), triple ($\sigma_{-1,2}$) ionization cross sections, and the sum (so-called detachment) ionization cross sections $\sigma_D = \sigma_{-1,0} + \sigma_{-1,1}$ for negative ions colliding with atomic and molecular targets (see, e.g., [9]). The electron affinities $I_{-1,0}$ (the first ionization potential) of negative ions for which experiments have been carried out are given in Table 4 for comparison.

Table 4. Electron affinities $I_{-1,0}$ (eV) for negative ions (from [8]).

Ion	$\boldsymbol{I_{-1,0}}$
B^-	0.277
C^-	1.26
O^-	1.46
F^-	3.40
Cl^-	3.61
Al^-	0.441
Si^-	1.389
S^-	2.08
Cu^-	1.235
Au^-	2.28

In Fig. 4, the experimental data on single-, double- and triple-ionization cross sections in C^- + Ar collisions are given as a function of relative velocity in comparison with the Firsov-model calculations. In the range of validity $v < 0.5$ a.u., the Firsov model predicts cross sections to be larger than the experimental data. Unfortunately, available experimental data obtained by different methods are not consistent. Therefore, it is quite difficult to make a reasonable comparison with the Firsov theory, though it is surely required to be improved extensively, for instance, using a more sophisticated atom-atom potential like the Biersack-Ziegler type (see section 2). Furthermore, more accurate experimental data should be pursued.

It should be pointed out that, in principle, one can also estimate single- and multiple-ionization cross sections of negative ions, neutrals and positive ions using semiempirical scaling laws [10] which have claimed a similar uncertainty of a factor of ~ 2 at high energy region. However, this scaling seems to be much more uncertain at low energy region.

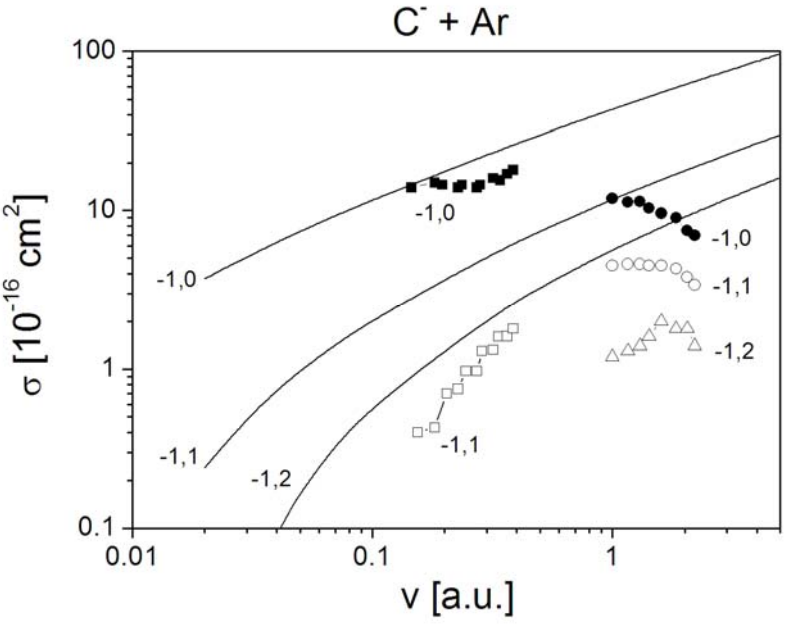

Fig. 4. Comparison of experimental data with the Firsov-model calculations for single-, double- and triple-ionization cross sections in C^- + Ar collisions: solid and open squares – experiment [11]; solid, open circles and open triangles – experiment [9]; solid curves – the Firsov model, eqs. (22) - (23).

4. Electron capture of Au ions in collisions with neutral atoms and ions. The CAPTURE code

In this work, the one-electron capture (EC) cross sections of ions colliding with neutral atoms and ions, eqs. (2) - (3), were calculated using the CAPTURE code described in [12,13]. Note that under the present collision situations where we estimate the charge changing processes in a tandem accelerator and beam attenuation in a plasma, multiple electron capture is not expected to be important and therefore is neglected.

Briefly, the CAPTURE code aims for calculating the probabilities P(b,v) and cross sections σ(v) for single-electron capture in ion-atom and ion-ion collisions, eqs. (2) - (3), as a function of the impact parameter b and the collision velocity v. It is based on normalized Brinkman-Kramers (BK) approximation in the impact parameter representation (see [14]). A total cross section is given by the sum of partial cross sections σ_n for all possible states with the principal quantum numbers n as a function of collision velocity v:

$$\sigma_{tot}(\mathrm{v}) = \sum_{\gamma} \sum_{\mathrm{n}_0}^{\mathrm{n}_{\mathrm{cut}}} \sigma_{\gamma n}(\mathrm{v}), \quad \sigma_{\gamma n}(\mathrm{v}) = 2\pi \int_0^{\infty} P_{\gamma n}^{(N)}(b,\mathrm{v})\, b\, db,$$

$$P_{\gamma n}^{(N)}(b,\mathrm{v}) = \frac{P_{\gamma n}(b,\mathrm{v})}{1 + \sum_{n'=n_0}^{n_{\max}} P_{\gamma n'}(b,\mathrm{v})} \quad , \qquad (24)$$

where $P_{\gamma n}(b,\mathrm{v})$ denotes the electron capture probability from the target shell γ into the n-state of the resulting ion, including the ground state n_0, at the impact parameter (b) and the collision velocity (v) in the BK approximation, $n_{\max}$ the maximum principal quantum number taken into account for the probability. The summation is also made over all shells of the target γ. Here N refers to the normalized probability and n_{cut} is a parameter depending on target density: for low-dense targets it is infinity while in a dense target it is strongly reduced due to the so-called *target-density effects* (see [13]).

In the CAPTURE code, the hydrogenic wave functions P_{nl}^{H} are used for a particle with a charge q:

$$P_{nl}^{q}(r) = Z_{scr}^{1/2}\, P_{nl}^{H}(Z_{scr} r), \quad Z_{scr} = n\sqrt{2I_{nl}(q)} \qquad (25)$$

where Z_{scr} is an effective charge to take account of the screening effects for the *nl* shell and I_{nl} denotes a binding energy of the target atom (ion), or the resulting ion $X^{(q-1)+}$. The hydrogenic wave functions here are used because of three main reasons as following:

1. At relatively low energies, the role of excited hydrogenic states is very large,
2. At high energies, the inner-shell target electrons close to nuclei are mainly captured and, therefore, can be described by the hydrogenic functions,
3. It is possible to get the capture probabilities in a closed analytical form expressed in terms of the McDonald functions $K_n(x)$ and to include excited states with n_{max} up to very high n ~1000.

The capture cross sections calculated by the CAPTURE code for reactions of interest at 3 MeV are presented in Table 5 and Figs. 5 – 8. In the case of H_2 targets, the cross sections were evaluated by using the semi-empirical law [15] obtained on the basis of numerous experimental data for electron capture in H and H_2 targets which reads:

$$\frac{\sigma_{H_2}}{\sigma_H} = \begin{cases} 0.76, & X < 6 \\ 0.76 + 0.0328\,(X-6), & 6 < X < 100 \\ 3.84, & X > 100 \end{cases} \qquad (26)$$

$$X = E(keV/amu)\cdot q^{-4/7}$$

where E and q denote the kinetic energy and charge of the projectile ion. The capture cross sections of highly charged ions on hydrogen atoms can be estimated by using a 'universal' curve also given in [15] which was obtained by using the Bohr-Lindhard [16] model for electron capture.

Table 5. Electron capture cross sections (10^{-16} cm^2) at the projectile energy of 3 MeV (calculated by the CAPTURE code).

	Au + H	**Au + He**	**Au + Ar**	**Au + Xe**	**Cu + Ar**
$\sigma_{0,-1}$	4.6	1.3	6.3	5.8	1.6
$\sigma_{1,0}$	19.0	9.0	24.0	30.0	9.0
$\sigma_{2,1}$	20.0	14.0	28.0	30.0	12.0
$\sigma_{3,2}$	13.0	18.0	21.0	15.0	17.0
$\sigma_{4,3}$	6.0	16.0	12.0	5.3	13.0

We note that 3 MeV energy corresponds to 15.2 keV/amu (v = 0.3 a.u.) for Au ions. This is a region of quite low energies where the capture cross sections strongly depend on energy defects ΔE, *i.e.*, differences in binding energies of the captured electron before and after collision: the lower ΔE value has the larger cross section. For example, the ΔE values for capture reactions of Au^+ ions on various atoms (the second row of Table 5) are, respectively, $\Delta E_{1,0}(H)$ = 13.6 – 9.23 = 4.37, $\Delta E_{1,0}(He)$ = 11.0, $\Delta E_{1,0}(Ar)$ = 2.2, and $\Delta E_{1,0}(Xe)$ = 1.5 eV. That is why the cross sections are largest for Xe target, a little bit smaller for Ar, and the smallest for He target. At relatively high collision energies E_c >> ΔE, capture cross sections do not depend on the energy defect ΔE but, instead, on the binding energies of the target inner-shell electrons (see, *e.g.*, [14]).

Figure 5 shows a comparison of the capture cross sections for C^+ + H collisions calculated by the CAPTURE code with recommended data presented in [14]; there is a reasonable agreement in the whole energy range.

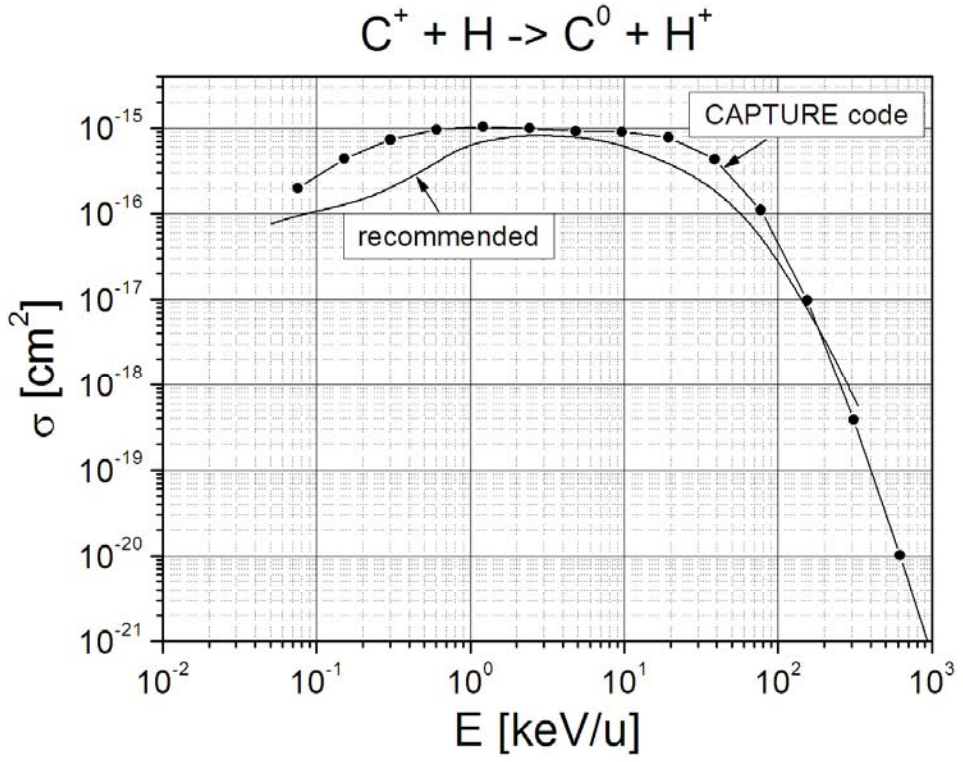

Fig. 5. Capture cross sections for C^+ + H collisions: solid curve – recommended data [14]; curve with solid circles – the CAPTURE code.

Calculated cross sections for electron capture of Au^{q+} and Cu^{q+} ions from Ar and Xe targets are given in Figs. 7 – 8. We note that the cross sections $\sigma_{0,-1}$ for reactions X^{0+} + A → X^- +

A^+ forming negative ions should also be accounted for in treating the charge fraction distributions because they are quite large and comparable with other cross sections (see sections 2 and 3)

Calculated one-electron capture cross sections for Au^+ and Au^{2+} ions from heavy particles such as H, H_2, He and He^+, which are important components of H and He plasmas, are given in Figs. 9 and 10. Again, the largest capture cross section corresponds to the reaction with the minimum energy defect ΔE, *e.g.*, among collisions of Au^+ ions the cross sections for reaction $Au^+ + H \rightarrow Au + H^+$ are the largest as it has the minimum energy defect $\Delta E_{1,0}(H) = 4.4$ eV.

.

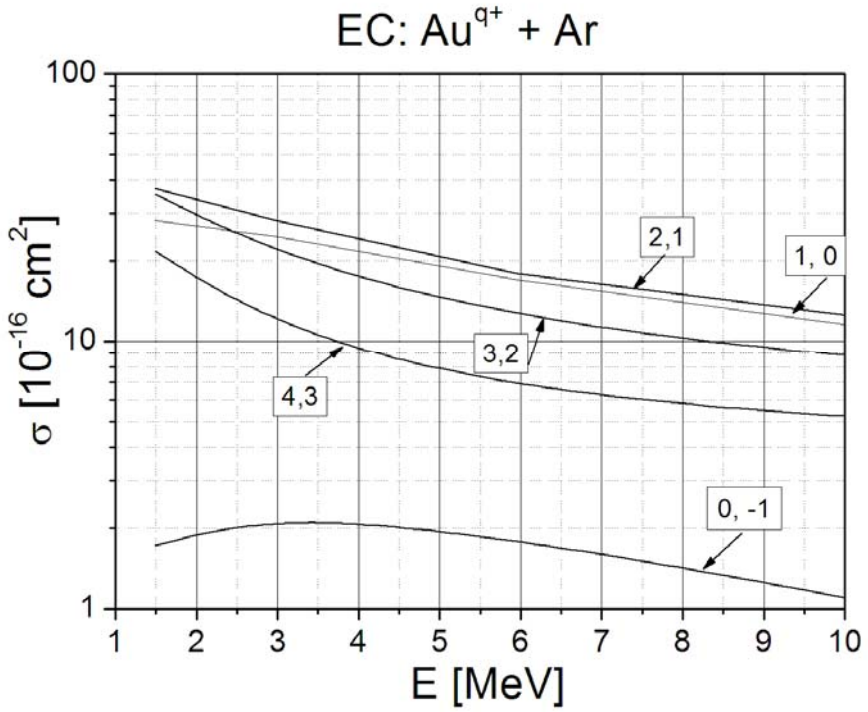

Fig. 6. Electron capture (EC) cross sections for Au^q + Ar collisions (q = 0 - 4) as a function of Au ion energy (CAPTURE code).

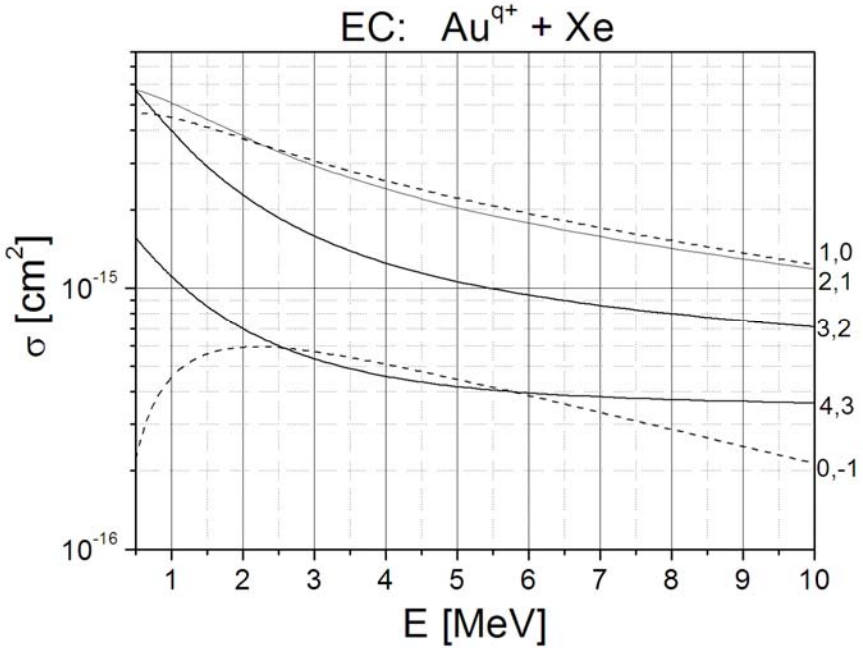

Fig. 7. Electron capture (EC) cross sections for Au^q + Xe collisions (q = 0 - 4) as a function of Au ion energy (CAPTURE code).

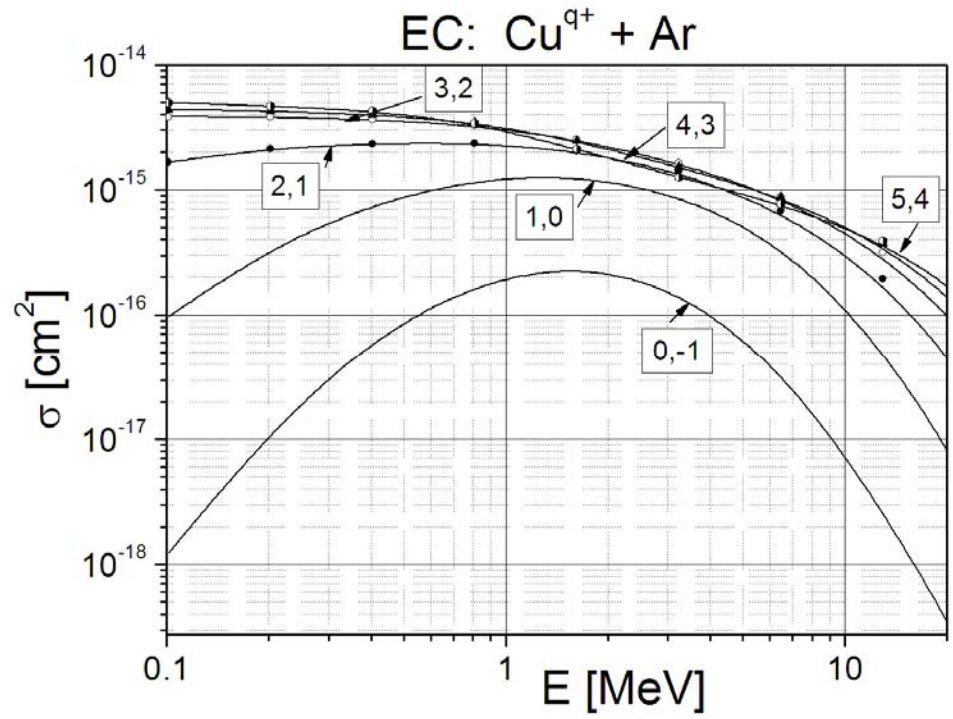

Fig. 8. Electron capture cross sections for Cu^q + Ar (q = 0 - 5) collisions as a function of Cu ion energy (CAPTURE code).

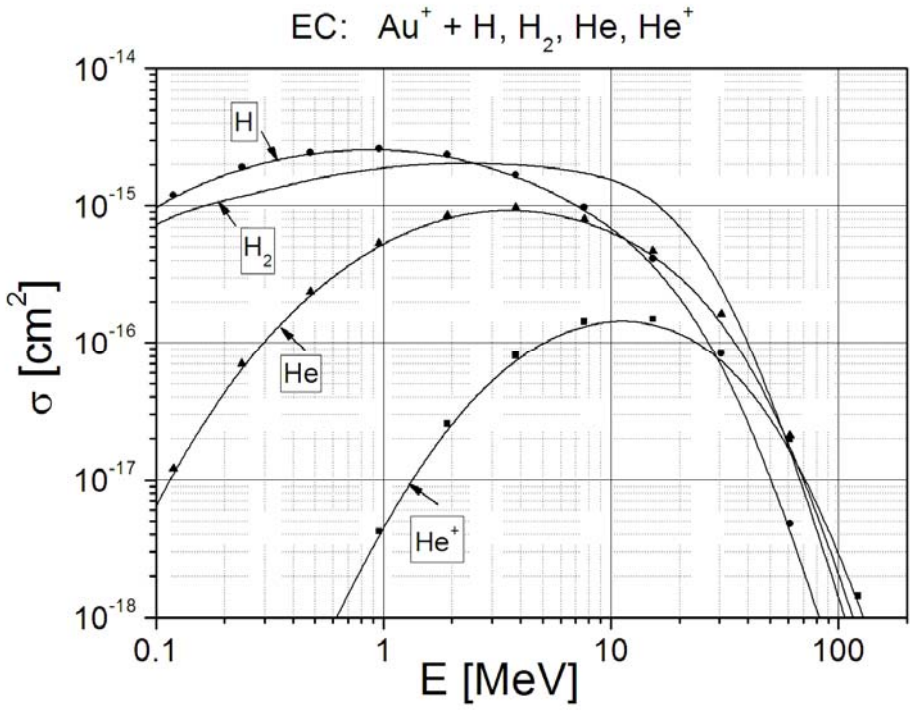

Fig. 9. Electron capture cross sections for $Au^+ + H$, H_2, He and He^+ collisions as a function of Au ion energy (CAPTURE code). For H_2 target, the cross section was estimated using eq. (26).

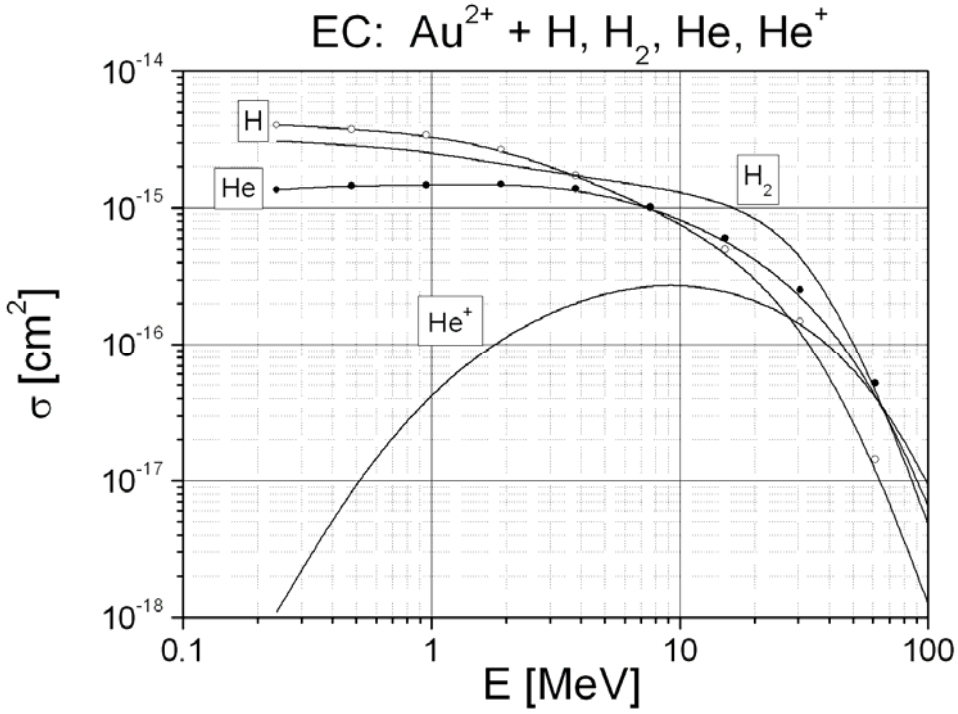

Fig. 10. Electron capture cross sections for $Au^{2+} + H$, H_2, He and He^+ collisions as a function of Au ion energy (CAPTURE code). For H_2 target, the cross section was estimated using eq. (26).

5. Optimization of Au^+ fractions in Au^- collisions with gases: application to HIBP

To optimize a fraction of exit Au^+ ions at 3 MeV, namely, to find the best target gas and areal gas density, one has to solve a set of differential equations describing rates of the exit Au ions in different charge states (see, *e.g.*, [17]). We note that such differential equations were solved in the earlier paper [18] but without taking account of the electron capture cross sections.

To make diagnostics of H and He plasmas with the HIBP technique, a beam of heavy Au^+ ions, obtained after Au^- ions passing through a gas cell, are accelerated up to 6 MeV and then injected into the plasma region. To estimate possible ion fractions after the gas cell, a six charge-state model was used in the present work, *i.e.,* taking six fractions F^{q+} of the exit ions into account, namely Au^-, Au^{0+}, Au^+, Au^{2+}, Au^{3+} and Au^{4+}, which can be obtained by solving six coupled differential rate equations including the electron-capture cross sections:

$$\frac{dF^-}{dx} = -F^-(\sigma_{-1,0} + \sigma_{-1,+1} + \sigma_{-1,2} + \sigma_{-1,3} + \sigma_{-1,4}) + \sigma_{0,-1} F^0 , \quad (27)$$

$$\frac{dF^0}{dx} = -F^0(\sigma_{0,-1} + \sigma_{0,1} + \sigma_{0,2} + \sigma_{0,3} + \sigma_{0,4}) + \sigma_{-1,0} F^- + \sigma_{1,0} F^+ , \quad (28)$$

$$\frac{dF^+}{dx} = -F^+(\sigma_{1,0} + \sigma_{1,2} + \sigma_{1,3} + \sigma_{1,4}) + \sigma_{-1,1} F^- + \sigma_{0,1} F^0 + \sigma_{2,1} F^{2+} , \quad (29)$$

$$\frac{dF^{2+}}{dx} = -F^{2+}(\sigma_{2,1} + \sigma_{2,3} + \sigma_{2,4}) + \sigma_{-1,2} F^- + \sigma_{0,2} F^0 + \sigma_{1,2} F^+ + \sigma_{3,2} F^{3+} , \quad (30)$$

$$\frac{dF^{3+}}{dx} = -F^{3+}(\sigma_{3,2} + \sigma_{3,4}) + \sigma_{-1,3} F^- + \sigma_{0,3} F^0 + \sigma_{1,3} F^+ + \sigma_{2,3} F^{2+} + \sigma_{4,3} F^{4+} , \quad (31)$$

$$\frac{dF^{4+}}{dx} = -F^{4+}(\sigma_{4,3} + \sigma_{4,5}) + \sigma_{-1,4} F^- + \sigma_{0,4} F^0 + \sigma_{1,4} F^+ + \sigma_{2,4} F^{2+} + \sigma_{3,4} F^{3+} . \quad (32)$$

Here $x = NL$ is the areal density with N being the target particle density (in particles/cm^3) and L the length of the gas cell (in cm).

Using the ionization and electron-capture cross sections calculated in the previous sections, the set of eqs. (27) - (32) were solved for different colliding systems using the Runge-Kutta method. Typical examples for Au^- - Ar and Cu^- - Ar collisions at 3 MeV are shown in Figs.

11 and 12 where calculated charge-state fractions are shown as a function of the areal density of target atoms.

Figure 11 clearly shows that, at higher gas pressures, the fraction of higher charge states increases steadily due to multiple collisions and may approach a real charge equilibrium at sufficiently high densities. Figure 11 also shows that at the present energy of 3 MeV the most favorable range of Ar atom density for production of Au^+ ions is around $(4 - 5) \times 10^{14}$ cm^{-2}. Similar trends can be seen in Fig. 12 for Cu ion collisions.

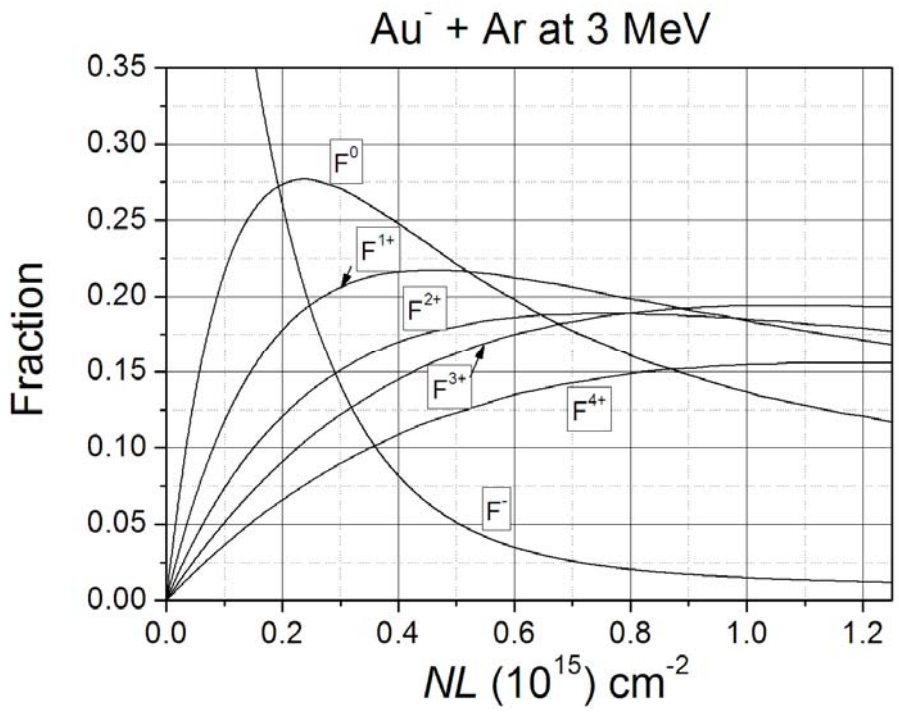

Fig. 11. Calculated charge-state fractions F^{q+} of Au^{q+} ions created in collisions of 3 MeV Au^- ions with Ar gas as a function of the gas areal density.

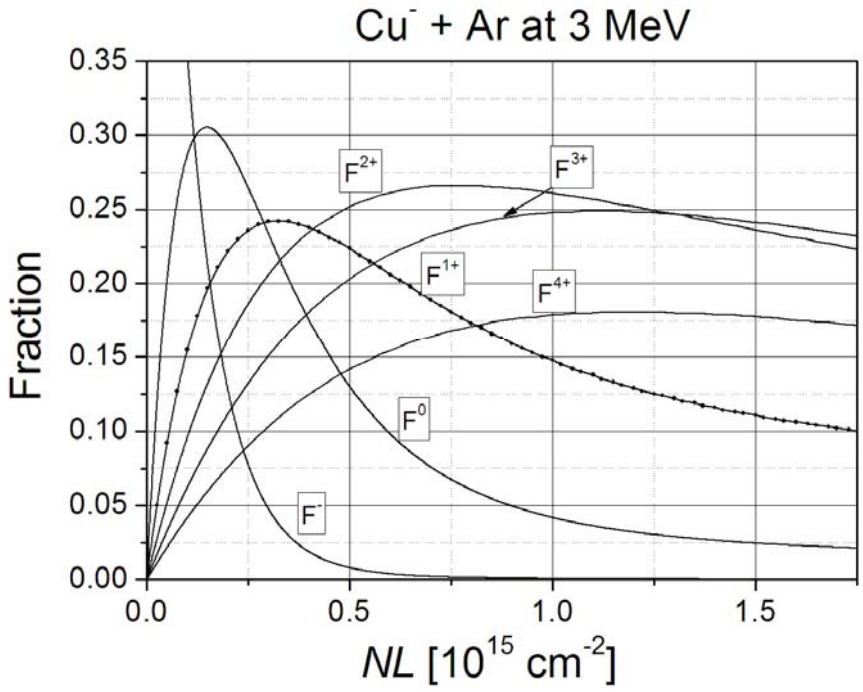

Fig. 12. Calculated charge-state fractions F^{q+} of Cu^{q+} ions created in collisions of 3 MeV Cu^- ions with Ar gas as a function of the gas areal density.

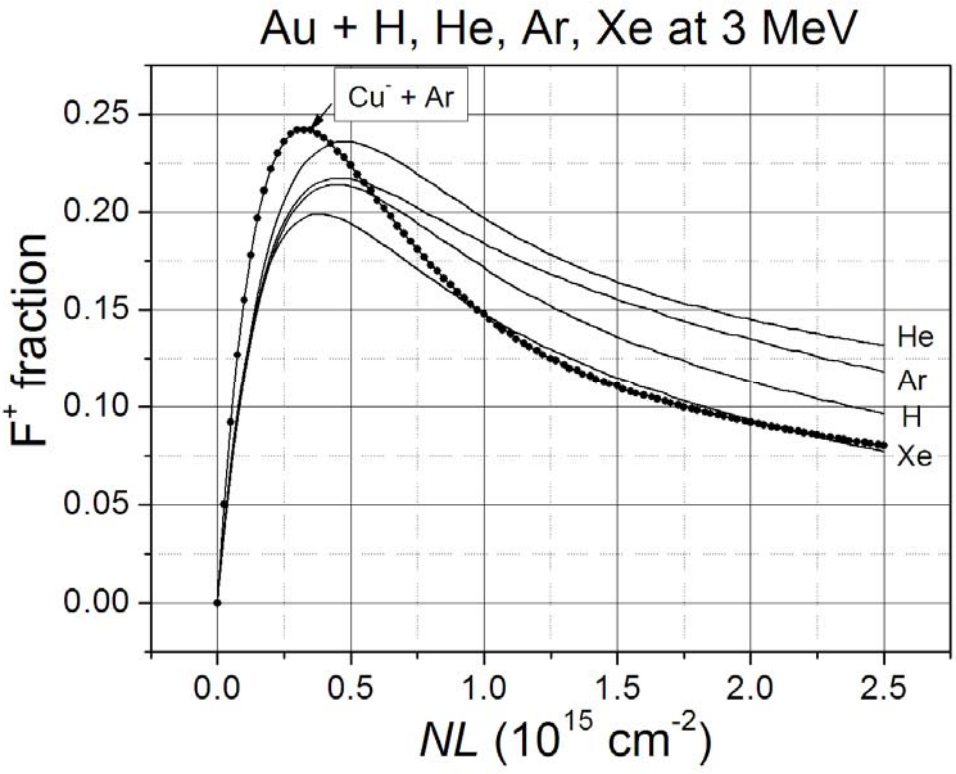

Fig. 13. Calculated charge-state fractions F^+ of singly charged ions in collisions of 3 MeV Au^- and Cu^- ions with noble gases as a function of the gas areal density.

Figure 13 shows the dependence of the optimum F^{1+} fractions of Au ions for different gas targets as a function of the target density calculated in the present work. According to Fig. 13, the best gas target to efficiently create singly charged Au^+ ions in Au^- - gas collisions at 3 MeV seems to be He at an areal density of about 5.0 x 10^{14} cm^{-2}, though th difference among gases is not so significant. Another candidate is Cu^- ion colliding with Ar atoms as also shown in Fig. 13. The highest fraction of Cu^+ ions can be reached at slightly lower gas pressures than for Au^+ ion.

As seen in Figs. 11 and 12, it is expected that 10 % fractions of total ion beam at the optimum gas pressures are missing mainly due to the omission of higher charge states (q ≥ 5). This is not serious for the present analysis as we do not intend to go to higher gas pressures. But we have to note that, in principle, we need to include q = 10 - 15 fractions into the differential rate equations (27) - (32) to provide more adequate conditions of particle conservation:

$$\sum_q F^{(q)} = 1 \ . \qquad (33)$$

However, we had to limit ourselves to only six fractions because it was not possible to calculate ionization cross sections by the Firsov model which is valid for ionization of only $m \le 4$ electrons. It should also be noted that the Firsov model can not be applied for highly charged ions (q >>1) as it uses the Thomas-Fermi potential between two neutral atoms (see section 2). The limited number of the charge fractions can lead to a partial loss of the projectile ions at higher target densities. For example, for Au^- - Ar collisions at 3 MeV, the sum $\sum_{q=-1}^{q=4} F^{(q)} \approx 1$ at $NL < 5 \times 10^{14}$ which is roughly optimum for Au^+ ion production. However, for $NL = 1.4 \times 10^{15}$ and 2.5×10^{15} cm^{-2}, the sum equals 0.8 and 0.6, respectively. The reason of this violation is that fractions with higher charge states ($q > 5$) are not accounted for in eqs. (27) – (32). Fortunately, in the region of maximum of F^{1+} fraction (Figs. 13 – 15), the sum, eq. (33), is close to unity and one can neglect the influence of higher charge-state fractions. This clearly shows a limitation of the present six-charge-state component model.

6. Ionization of Au ions by light low-charged ions (plasma constituents). The LOSS code

Now Au^+ ions accelerated up to 6 MeV are injected into the main plasmas to measure the plasma potential inside, as explained above, and then encounter with the plasma constituent particles.

For ionization of heavy Au and Cu ions by low-charged few-electron light ions in H- and He-plasmas (protons, He^+ and He^{++}), the Firsov model, described in the section 3, can not be

used. In such cases, the LOSS code [12] was used in the present work. In short, the LOSS code aims for calculating the single-ionization (SI, eq. (1)) cross sections of projectiles by target atoms and ions. It is based on the first non-relativistic Born approximation by using the Schrödinger radial wave functions calculated numerically with the ATOM code [19]. In the present work, ionization cross sections by electron impact were also calculated by the ATOM code.

In the LOSS code, the ionization cross section in the partial-wave representation is written as,

$$\sigma_{\mathrm{ion}}(\mathrm{v}) = \frac{8\pi}{\mathrm{v}^2} \sum_{\mathrm{P}} \sum_{\lambda} \int_0^{\infty} d\varepsilon \int_{\mathrm{Q_{min}}}^{\infty} \frac{\mathrm{dQ}}{\mathrm{Q}^3} \left|F_P(Q,\varepsilon,\lambda)\right|^2 \cdot \left|F_T(Q)\right|^2, \tag{34}$$

where Q denotes the momentum transfer, ε and λ the energy and orbital momentum of an ejected electron, I_P the binding energy of the projectile electron shell, $Q_{\mathrm{min}} = (I_P + \varepsilon)/2\mathrm{v}$. The projectile form-factor is given by

$$\left|F_P(Q,\varepsilon,\lambda)\right|^2 = \left|\left\langle \varepsilon \left| \exp(i\vec{Q}\vec{r}) \right| 0 \right\rangle_P \right|^2 \tag{35}$$

and the effective charge of the target atom

$$\left|F_T(Q)\right|^2 = \left[Z_T - \sum_{j=1}^{N} \left\langle j \left| \exp(i\vec{Q}\vec{r}) \right| j \right\rangle \right]^2 + \left[N - \sum_{j=1}^{N} \left| \left\langle j \left| \exp(i\vec{Q}\vec{r}) \right| j \right\rangle \right|^2 \right]. \tag{36}$$

Here Z_T and N denote the nuclear charge and number of electrons of the target, respectively. In the LOSS code, the factor $F_T(\mathrm{Q})$ is calculated by using the nodeless Slater wave functions.

The results of calculated ionization cross sections of Au ions by electrons, protons, H, He atoms and their ions (He^+ and He^{2+}: the main components in He plasmas), as well as by carbon atoms and ions (the main impurities in plasmas)) are given in Figs. 14 – 16 as functions of Au ion energy. Calculated single-ionization cross sections of Au^+ ions by protons and C^{q+} ions as functions of Au ion energy are given in Fig. 15 to show possible influence of impurity carbon ions on the overall effective ionization cross sections. Note that the ionization cross sections are more than one order of magnitude larger in C^{6+} ion collisions than in protons, indicating that even a small fraction of such impurity ions are important in hot plasmas.

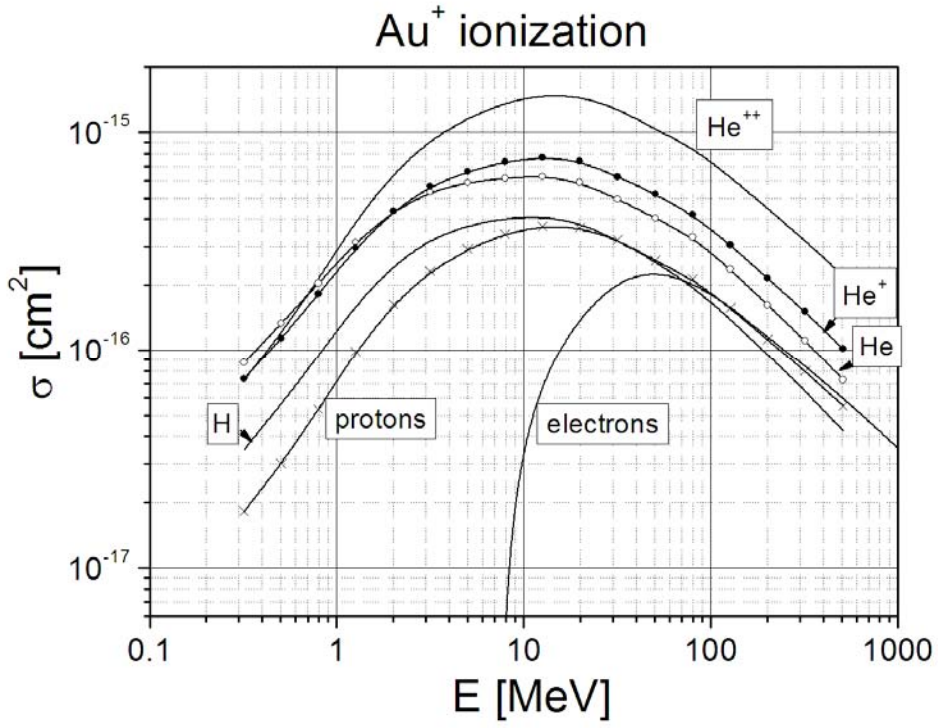

Fig. 14. Calculated single-ionization cross sections of Au^+ ions by electrons, H atoms, protons, He atoms and its (He^+ and He^{2+}) ions as a function of Au ions (LOSS code). The electron impact ionization cross section is plotted in the scale of equivalent Au energy.

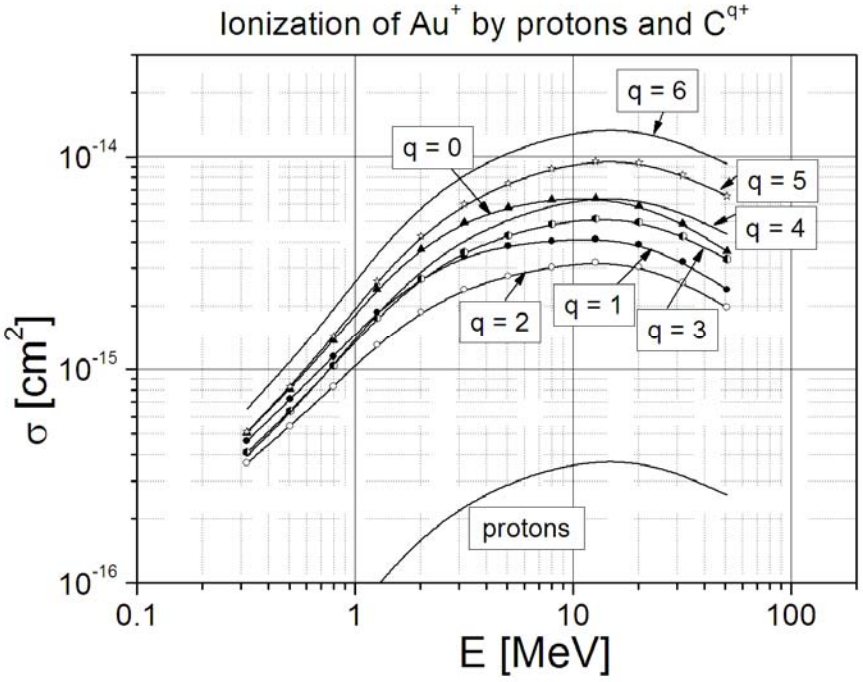

Fig. 15. Calculated single-ionization cross sections of Au^+ ions by protons and C^{q+} (q = 0 – 6) ions as a function of Au ion energy (LOSS code).

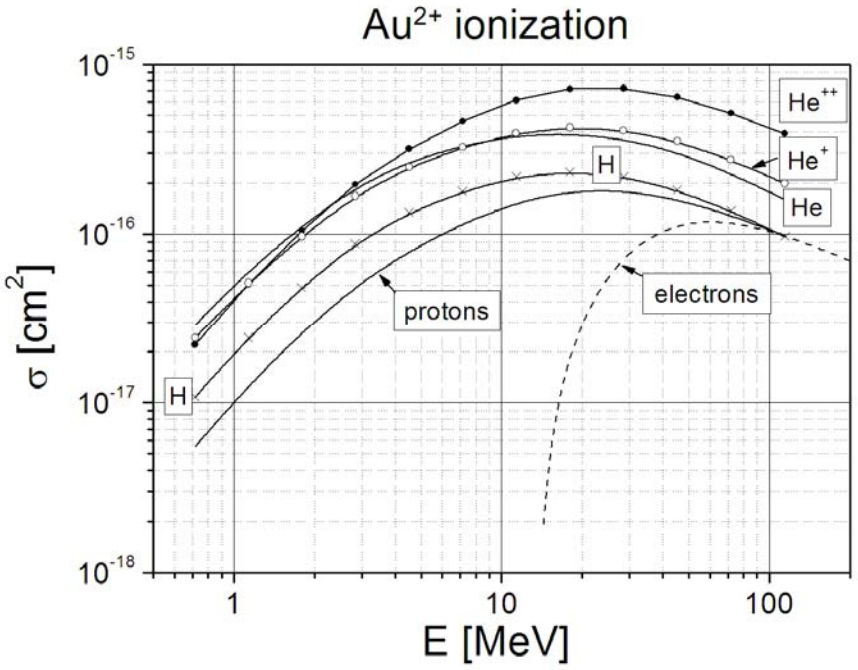

Fig. 16. Calculated single-ionization cross sections of Au^{2+} ions by electrons, protons, H, He atoms and their ions (LOSS code). The electron-impact ionization cross section is plotted as a function of the equivalent electron energy.

For ionization of Au ions by H and He atoms, the LOSS code gives results close to the Firsov model within a factor of 2 at velocities v = 0.75 – 1.1 a.u. (the velocity range of the present LHD-HIBP setup corresponding to the energy range of 1.5 – 6 MeV) as it is shown in Fig. 19 (left panel) for ionization of Au^+ ions by He atoms. On the other hand, in the case of heavy targets and low energies, the LOSS code can not be applied because it is based on the first Born approximation which fails to reproduce the observed data (see, *e.g.*, [20]). This feature is clearly demonstrated on the right panel in Fig. 17 for ionization of Au^+ ions by Ar atoms.

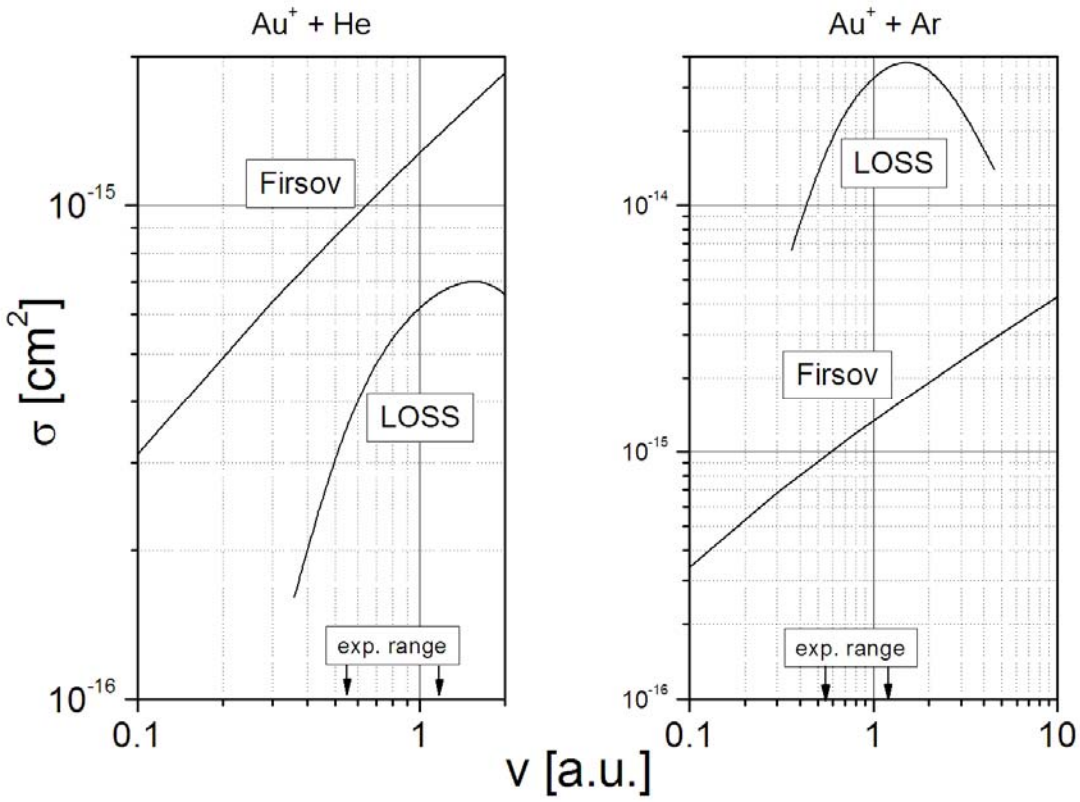

Fig. 17. Calculated single-ionization cross sections of Au^+ ions by He and Ar atoms as a function of Au ion velocity: labels *Firsov* and *LOSS* refer to the Firsov model, eqs. (22) - (23), and the LOSS code (see text). *Exp. range* is the ion energy range of 1.5 – 6 MeV (v = 0.55 – 1.1 a.u.) presently used at LHD-HIBP setup.

Finally, we have to consider ionization of Au^+ and Au^{2+} projectiles through electron capture by H^+, He^+ and He^{2+} (the main H- and He-plasma particles) (eq. (3), IEC). The corresponding cross sections, calculated by the CAPTURE code, are shown in Figs. 18 – 19. It is seen that at the present energy (6 MeV) this channel of ionization of Au ions (by the target-ion electron capture) is even more effective than the direct ionization process, eq. (1), (c.f. Figs. 14 - 16) and should be taken into account in analysis of the losses of the injected Au^+ ions into plasmas.

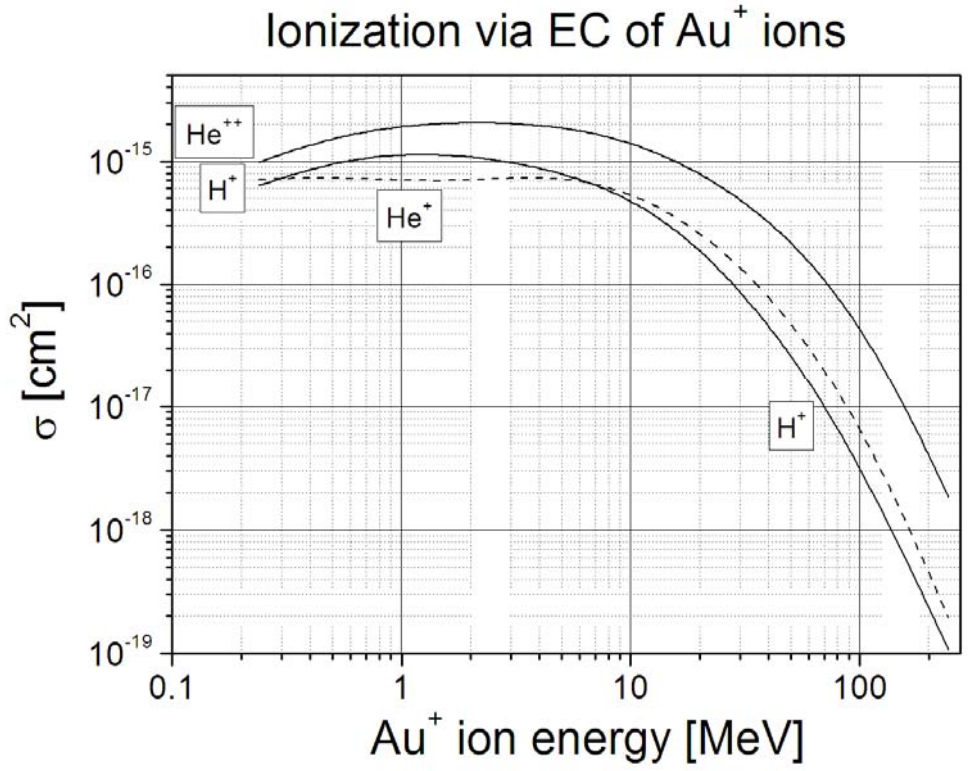

Fig. 18. Ionization of Au^+ projectiles through electron capture by H^+, He^+, and He^{2+} (the main H- and He-plasma particles) (eq. (3), IEC), calculated by the CAPTURE code.

7. Recombination of Au ions in plasmas. Dependence on electron temperature

In plasmas, recombination of projectile ions occurs not only through capture of the bound electrons belonging to atoms, ions and molecules, but also by capture of free electrons. Recombination of a free electron takes place mainly via the following three processes:

a) Photorecombination (radiative recombination: RR)

$$X^{q+} + e \rightarrow X^{(q-1)+}(nl) + \hbar\omega \qquad (37)$$

An electron is captured into an *nl*-state of ion, meanwhile excess energy is emitted as a photon ($\hbar\omega$).

b) Three-body (or ternary) recombination which is an inverse process to ionization:

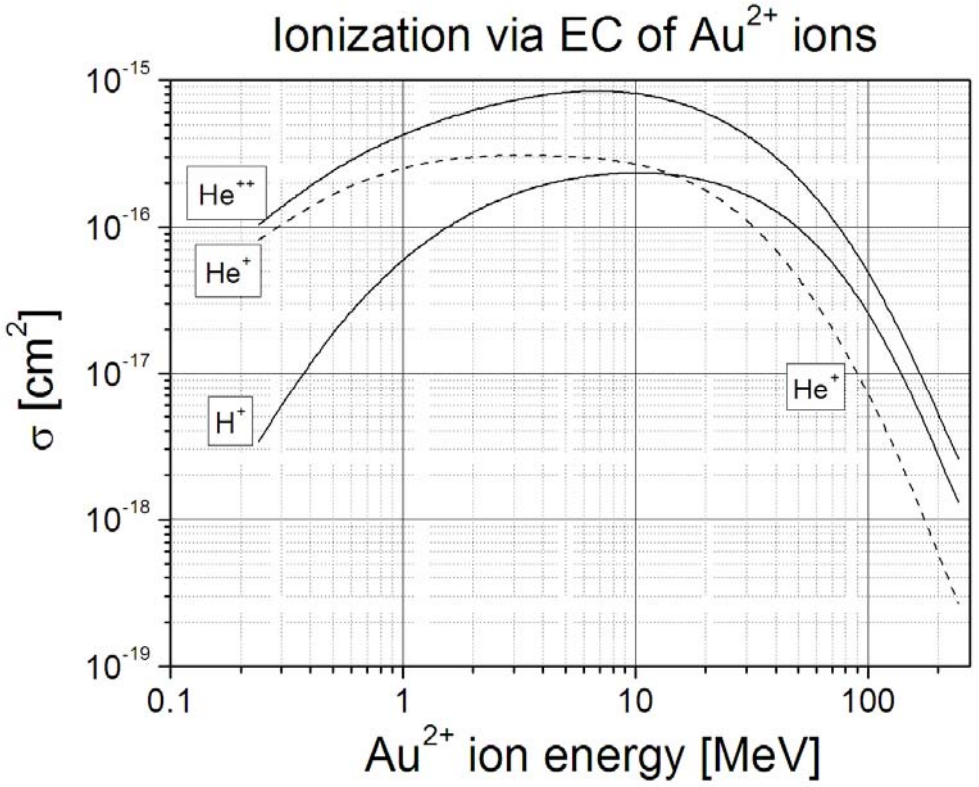

Fig. 19. Ionization of Au^{2+} projectiles through electron capture by H^+ and He^+ and He^{2+} (the main H- and He- plasma particles) (eq. (3), IEC), calculated by the CAPTURE code.

$$X^{q+} + e + e \rightarrow X^{(q-1)+}(nl) + e \ , \tag{38}$$

and

c) Dielectronic recombination (DR):

$$X^{q+} + e \rightarrow \left[X^{(q-1)+}\right]^{**} \rightarrow X^{(q-1)+}(nl) + \hbar\omega \ , \tag{39}$$

where an incident ion captures a free electron and simultaneously one of inner-shell electrons in the ion is resonantly excited into higher states, forming intermediate doubly excited states $X^{(q-1)+**}$. Then, the intermediate state is stabilized to the ground state via photon emission ($\hbar\omega$). The DR peak cross sections, eq. (39), are generally very large, compared with those for the RR. However, integrated cross sections are much smaller due to the resonance features, except for very heavy, highly charged ions.

The ternary process (38) is important only in high-density, low-temperature plasmas. The DR is an important recombination process for highly charged ions if the relative velocity v_r is high enough to excite an inner-shell projectile electron (see, *e.g.*, [21]).

The monoenergetic free-electron recombination cross section, eq. (37), into a specific state with the principal quantum number n is well described by the semiempirical formula [22] obtained on the basis of numerical calculations and the Kramers formula:

$$\sigma(n)=\frac{2.1\times10^{-22}\ cm^2}{n^3}\frac{Z_{eff}^4}{E_e(E_e+Z_{eff}^2/n^2)},\quad Z_{eff}=(Z+q)/2\ , \tag{40}$$

where Z and q denote the nuclear charge and ion charges of the incident projectile ion, and E_e the incident electron kinetic energy in Rydberg units (= 13.606 eV). In the case when resulting ions $X^{(q-1)+}$ are not hydrogenic, the cross section, eq. (40), should be multiplied by a statistical weight W(n) of the n shell, *i.e.*, on ratio between the number of unoccupied states and the total number $2n^2$ of possible states for a given n. For the hydrogenic states, W(n) = 1.

The total recombination cross section in collisions at the relative electron energy E_e is then given by

$$\sigma_{tot}=\frac{2.1\times10^{-22}\ cm^2}{n_0^2}\frac{Z_{eff}^4}{E_e(E_e+Z_{eff}^2/n_0^2)}W(n_0)+\sum_{n\geq n_0+1}\sigma(n)\ , \tag{41}$$

where n_0 denotes the ground state of the product $X^{(q-1)+}$ ion. Here the first term is concerned with the ground state and the second term to those for higher (excited) n-states which are treated as hydrogenic ones.

The sum over these hydrogenic states in eq. (41) is also well described by another formula [21]:

$$\sum_{n\geq n_0+1}\sigma(n)\approx 2.1\times10^{-22}cm^2\ \cdot\frac{u}{2}\cdot\ln\left(1+\frac{u}{(n_0+1)^2}\right),\ u=\frac{Z_{eff}^2}{E_e/Ry}=\frac{Z_{eff}^2}{\mathrm{v}_r^2}\ . \tag{42}$$

If an ion with velocity v_P passes through a plasma with electron temperature T_e, the relative electron energy E_e can be estimated by (see, e.g., [21]):

$$E_e=m\mathrm{v}_r^2/2=m(\mathrm{v}_P^2+\mathrm{v}_{th}^2)/2 \tag{43}$$

where m is the electron mass and v_{th} is the thermal electron velocity

$$\mathrm{v}_{\mathrm{th}} = \sqrt{\frac{8kT_e}{\pi m}} \approx 1.13\sqrt{T_e / Ry} \tag{44}$$

If $\mathrm{v_P} >> \mathrm{v_{th}}$, the corresponding total recombination rate coefficient can be calculated straightforward:

$$\kappa_{RR}(T_e) = \mathrm{v_r}\sigma_{tot}(\mathrm{v_r}) \ [cm^3 / s] \quad . \tag{45}$$

However, in general cases, in calculating the rate coefficient of a certain elementary process one has to take into account a Maxwellian velocity distribution of plasma electrons. Thus, the Maxwellian-averaged rate coefficient is given:

$$< \mathrm{v}\sigma(\mathrm{v}) > = \int \mathrm{v}\sigma(\mathrm{v})\, F(\mathbf{v}, T_\mathrm{e})\, d^3\mathbf{v} \tag{46}$$

where

$$F(\mathbf{v}, T_e)\, d^3\mathbf{v} = \left(\frac{m}{2\pi T_e}\right)^{3/2} \exp\left(-\frac{m\mathrm{v}^2}{2T_e}\right) d\varphi \ \sin\theta\, d\theta \ \mathrm{v}^2\, d\mathrm{v} \tag{47}$$

Introducing the relative velocity vector $\mathbf{v} = \mathbf{v}_\mathrm{e} - \mathbf{v}_\mathrm{P}$, where $\mathbf{v}_\mathrm{e}$ is the velocity vector of a plasma electron, and taking into account that $d^3\mathbf{v}_\mathrm{e} = d^3\mathbf{v}$, the rate coefficient can be written in a more general form:

$$< \mathrm{v}\sigma(\mathrm{v}) > = \left(\frac{m}{2\pi T_e}\right)^{3/2} \int_0^\infty \mathrm{v}\sigma(\mathrm{v}) \exp\left(-\frac{m(\mathbf{v}+\mathbf{v_P})^2}{2T_e}\right) d^3\mathbf{v} =$$

$$= \left(\frac{m}{2\pi T_e}\right)^{3/2} \exp\left(-\frac{m\mathrm{v}_\mathrm{P}^2}{2T_e}\right) \int_0^\infty d\mathrm{v}\, 2\pi\, \mathrm{v}^3\sigma(\mathrm{v}) \exp\left(-\frac{m\mathrm{v}^2}{2T_e}\right) \int_0^\pi \sin\theta\, d\theta \exp\left(-\frac{m\mathrm{v}_\mathrm{P}\,\mathrm{v}\cos\theta}{T_e}\right) =$$

$$= \left(\frac{2m}{\pi T_e}\right)^{1/2} \frac{1}{\mathrm{v_P}} \exp\left(-\frac{m\mathrm{v}_\mathrm{P}^2}{2T_e}\right) \int_0^\infty \mathrm{v}^2\sigma(\mathrm{v}) \sinh\left(\frac{m\mathrm{v}\mathrm{v}_\mathrm{P}}{T_e}\right) \exp\left(-\frac{m\mathrm{v}^2}{2T_e}\right) d\mathrm{v} \tag{48}$$

where *sinh* is a hyperbolic sinus:

$$\sinh x = \frac{e^x - e^{-x}}{2} \quad . \tag{49}$$

In Fig. 20 the total calculated rate coefficients for recombination of Au^+ ions on free electrons as a function of the plasma electron temperature T_e are given at projectile energy of 6

MeV, *i.e.,* v_P = 1.1 a.u. using eq. (45) and exact one (48) with radiative recombination cross sections σ(v) from eqs. (41) - (42). One can see that at electron temperatures T_e > 200 eV, the exact formula (48) gives values more than a factor of 2 larger than those from eq. (45).

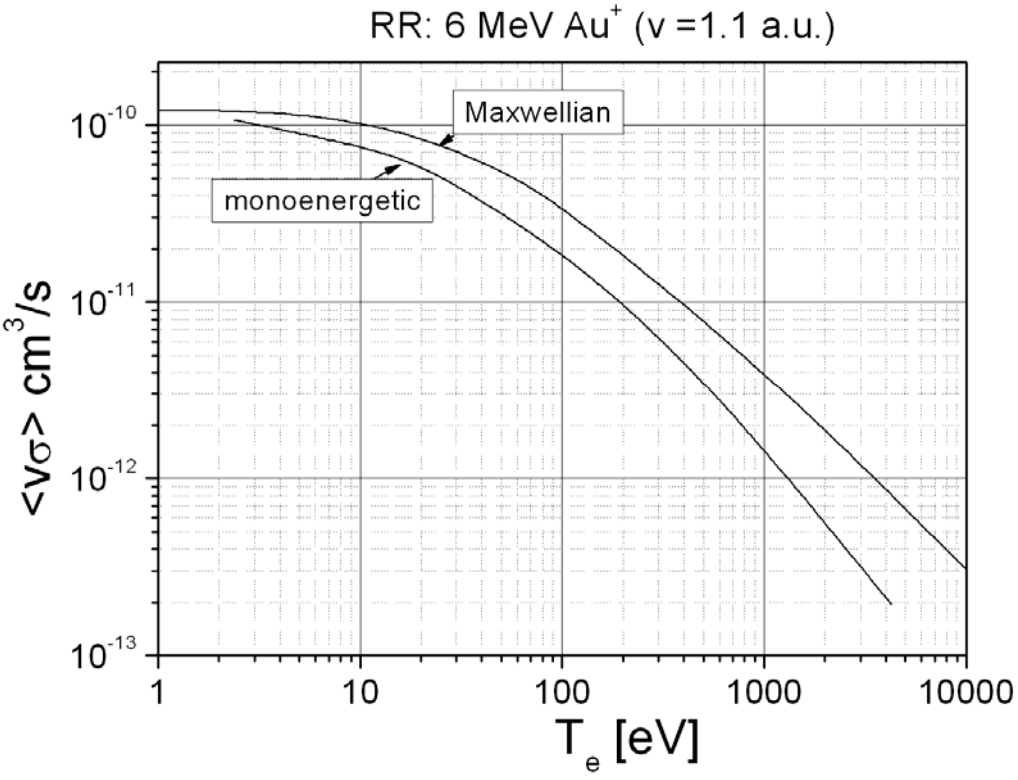

Fig. 20. Comparison of recombination rates of 6 MeV Au^+ ions (v = 1.1 a.u.) on plasma electrons as a function of the electron temperature: monoenergetic – eqs. (41), (42) and (45), Maxwellian – eqs. (41), (42) and (48). At electron temperature T_e > 100 eV, the difference between two curves becomes significant.

It is important to note that recombination rates of projectile ions with plasma (free) electrons is much smaller compared with those of recombination (electron capture) of the bound atomic electrons (see eq. (4)). A comparison of recombination of Au^+ ions on free electrons of H plasma and the bound electrons of cold H atoms and H_2 molecules is shown in Fig. 21. The difference is very large already at relative energies higher than 0.3 MeV (1.5 keV/amu), increasing drastically as the ion energy increases. In fact, the free electron recombination rates are completely negligible at 6 MeV Au^+ ion collisions.

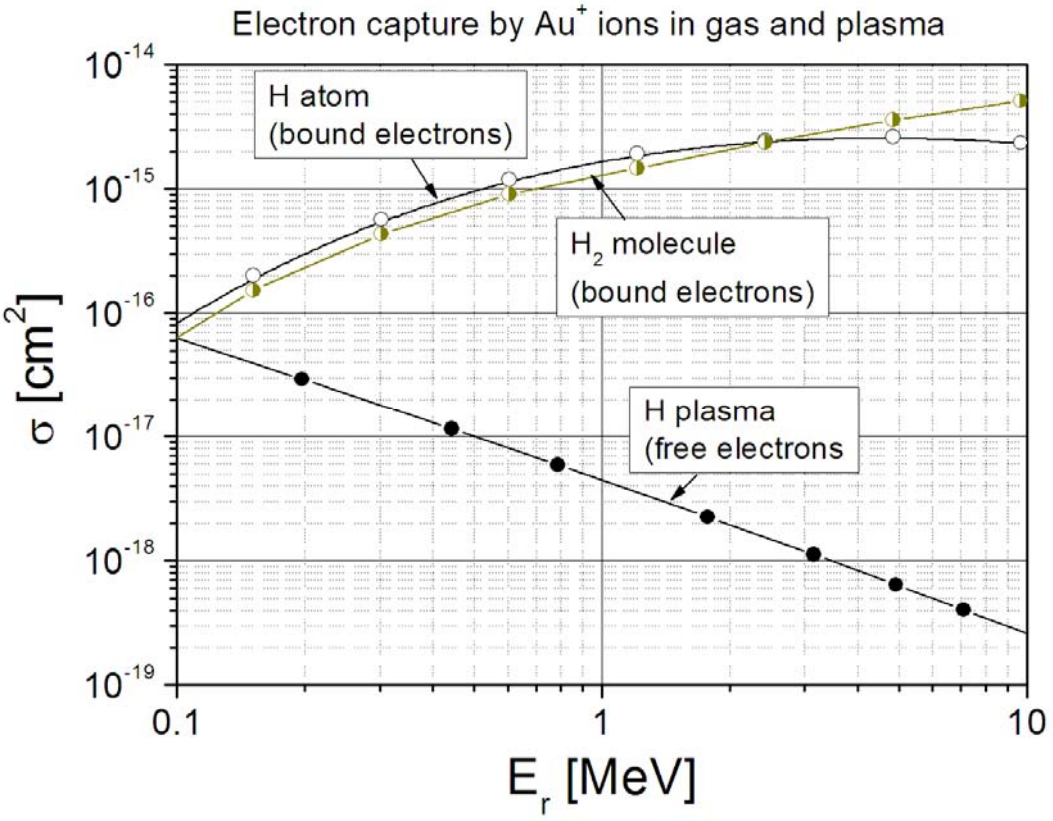

Fig. 21. Calculated total recombination cross sections of Au^+ ions in H and H_2 gases (H atoms - CAPTURE code, H_2 molecules – eq. (23)) and those in H plasma under condition $v_r \sim v_P$ (eqs. (41), (42), (45)) as a function of relative energy $E_r = mv_r^2$, eq. (43).

If the projectile velocity is higher than the thermal electron velocity, $v_P >> v_{th}$, the rate of three-body (or ternary) recombination, eq. (38), can be estimated by the formula ([21]):

$$K_{TR} = 2.92 \cdot 10^{-31}\ [cm^3/s]\ q^3\ N_e(cm^{-3}) / v_r^9(a.u.) \qquad (50)$$

where q denotes the incident ion charge, N_e the electron density and v_r the relative velocity given by eq. (43). In the case of low-charged ions colliding with the electron of density $N_e = 10^{16} - 10^{18}$ cm^{-3} like in typical Tokamak plasmas, the contribution of three-body recombination, eq. (38), is also negligible compared to photorecombination.

8. Beam attenuation dynamics in plasmas

Figure 22 shows schematically the whole system including the ion production, ion beam transport and ion detection system of HIBP in LHD. Briefly, Au^- ions produced in an ion source are transported into a 3 MV terminal voltage tandem accelerator, where they collide with gas target atoms at its positive voltage terminal and, then, after stripping off a few electrons, are further accelerated up to 3(q + 1) MeV energy (q: the ion charge after stripping). Among the ions, 6 MeV Au^+ ions are charge-separated and focused through a series of the lens systems and then sent into the LHD plasma region. First, these primary Au^+ ions, steered into the vacuum chamber of LHD, collide with relatively cold plasmas near the edge and, then, with a central plasma region to obtain information on the plasma parameters, where the main collisions of the primary Au^+ ions with the hot, dense central plasmas occur and a small fraction of them are converted to Au^{2+}. These secondary Au^{2+} ions are separated with the main magnetic field (~ 3 Tesla) and take their paths different from the primary Au^+ ions into the energy analyzing system (tandem energy analyzer in Fig. 22) and finally reach a micro-channel plate (MCP) detector located in the energy analyzer. On the other hand, the non-interacted primary Au^+ ions reach another detector whose current is used to normalize the secondary ion intensities.

All the way from the injection to the plasma center, the injected primary Au^+ ions collide with various plasma particles including H, H^+, (He, He^+ and He^{2+} in helium plasmas), electrons and may change their charge, energy and path and a fraction of them are lost. Furthermore, the charge-converted secondary Au^{2+} ions at the center plasma region encounter with similar plasmas down to the plasma edge region. To get the detailed information, such losses of the primary and also secondary ions have to be carefully taken into account.

In the previous sections, the cross sections necessary to obtain such information on the plasmas have already been calculated and given in a series of Tables and Figures.

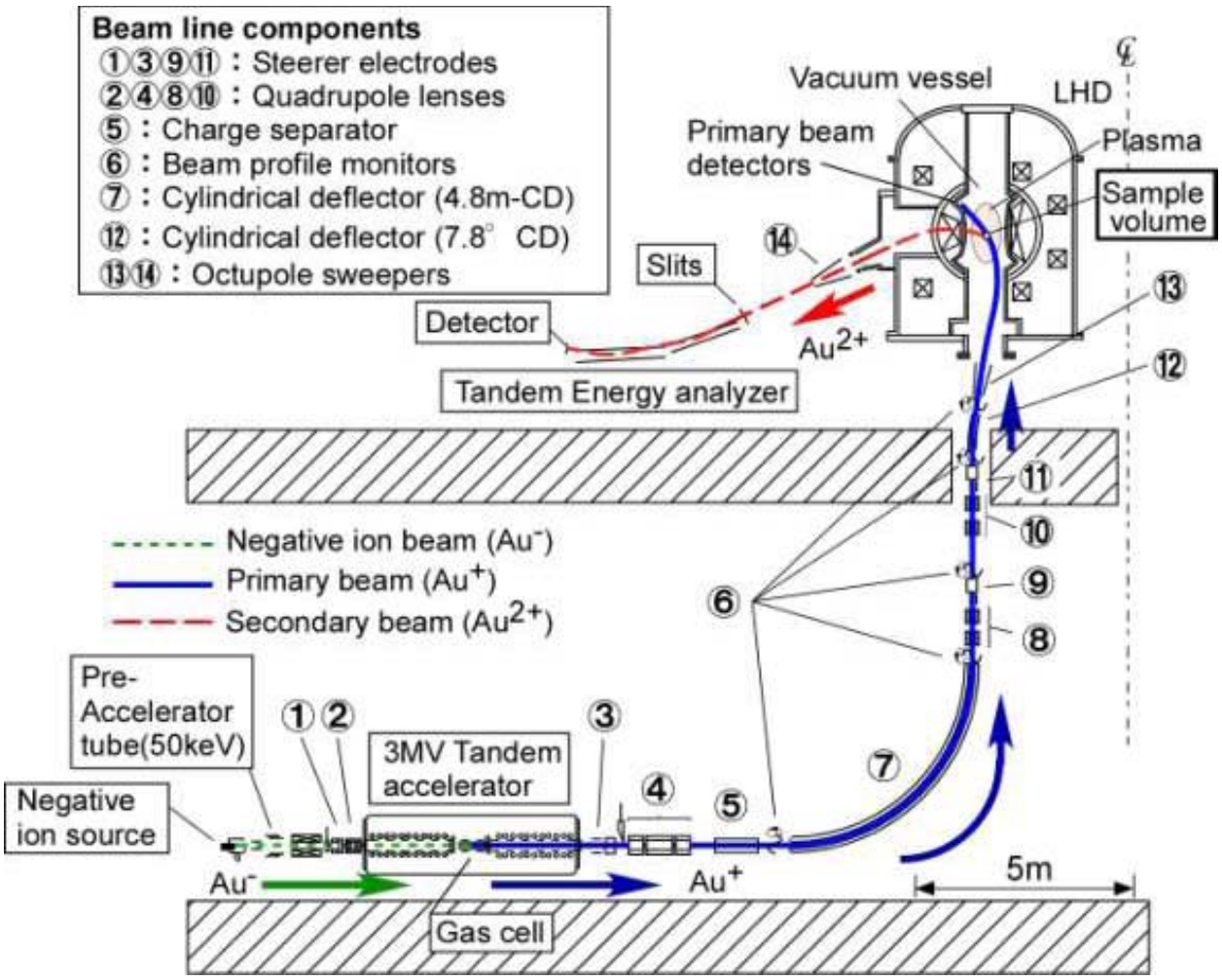

Fig. 22. Beam injection and detection system of HIBP in LHD.

8.1. Charge distributions at the exit of the tandem accelerator

So far only a limited experiments involving HIBP have been performed at LHD. One of them [23] is to investigate the charge fractions of Au^{q+} after Au^- ions collide with Ar gas atoms at 3 MeV at the accelerator terminal, which are shown in Fig. 23 as a function of the target thickness. It is clear that Au^+ ions are the most dominant at the gas pressure of p ~ 7 – 8 (relative target thickness) and at higher gas pressures Au^{2+} ions become dominant. This feature has already been shown in Fig 11, where the expected charge fractions are demonstrated against the gas density. Note that the relative calculated fractions include the neutral beam fractions but not ions with higher charges ($q \geq 5$), meanwhile the experiments do not all of them as well as Au^{4+} ions. The observed charge fractions generally show similar tendency as the calculated charge fractions. The maximum charge fraction of Au^+ does not reach the calculated value of ~ 0.22. This is because the output beam focusing for passing through the tandem accelerator is not optimized

enough. In recent experiments, however we have confirmed that the beam fraction of Au^{+} reaches almost the theoretical value of about 0.2 by adjusting the beam optics. Therefore this difference in the charge fractions should not be taken too seriously as the detection efficiencies and others are not well established yet, and thus, it is believed that the present cross sections given in this paper are reasonably accurate and seem to be encouraging for further detailed investigations.

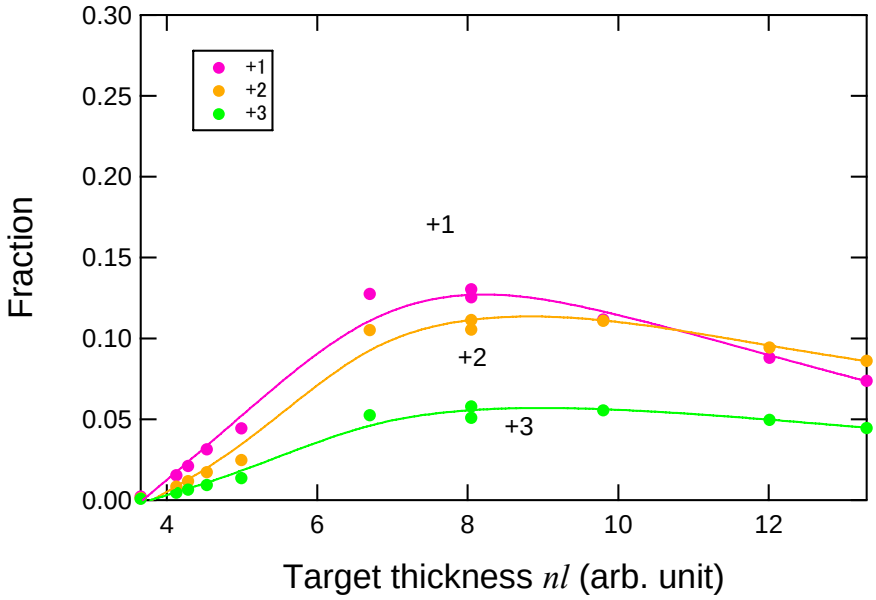

Fig. 23. Measured fractions of Au^{q+} ions after collisions with Ar gas atoms. The projectile Au^{-} ion energy is 3 MeV. These fractions have been measured at the terminal of the accelerator. The general features are quite similar to each other. The target thickness is corrected by the reading of the vacuum pressure gauge at the exit of the tandem accelerator.

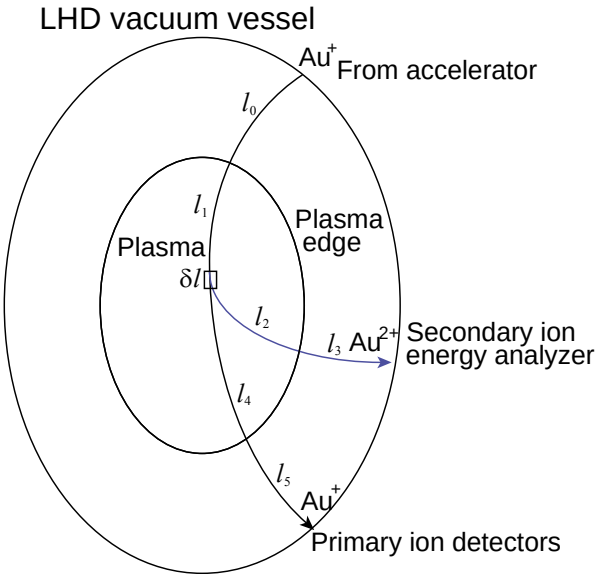

Fig. 24. Schematic geometry of the ion paths and their interacting lengths for estimation of the beam attenuation I_{B2}/I_{B0} of Au ions taking into account various collision processes with plasma particles in the LHD plasmas. The primary Au^+ ions collide, first, with relatively cold edge plasmas over the length of l_0 and, then, with the main hot dense plasmas along l_1. At the very plasma center, the primary Au^+ ions interact with the main plasmas over a short length (δl) and a part of them are converted to Au^{2+} ions which, then, move through the main plasma over l_2 and pass again through the edge plasmas (l_3) before reaching a detector. The rest of the non-interacted Au^+ ions goes through different path (l_4, l_5) to reach a primary ion detector.

8.2 Beam attenuation in plasmas

In the central plasmas, electrons, H^+ ions, as well as C^{6+} ($n_{C6+} \sim 1/30 \cdot n_e$ in the LHD plasmas) exist, meanwhile neutral particles such as H and H_2 (and possibly some hydrocarbon molecules) are present in the edge plasma region. Furthermore, He, He^+ and He^{2+} ions have to be taken into account in a helium plasma. The exact knowledge of the beam attenuation of the injected primary Au^+ and secondary product Au^{2+} ions through the main as well as the edge plasmas is essential to obtain accurate quantitative information on the plasma potential distributions, density and their variations of the central plasmas through the present HIBP method and, in its detailed analysis, we should include all the possible collision processes involving electrons, ions and neutral particles which are always present in the plasmas, as already pointed out previously.

Now these cross sections obtained in the previous sections are applied to such analyses of the plasmas of LHD. The attenuation of the injected primary ion beam density, n_B, due to the

ionization processes per unit path length l while passing through the central, hot plasma is given, assuming that their distributions are uniform along the ion paths, by

$$v_B \frac{dn_B}{dl} = -n_e n_B \left\langle \sigma_{ei}^{1,2} v_e \right\rangle - n_{H^+} n_B \left\langle \sigma_{loss}^{1,2} v_B \right\rangle, \tag{51}$$

where v_B is the ion velocity, n_B, n_e and n_{H+} represent the densities of Au^+ ions, electrons, and protons, respectively. Here the first term on the right-hand side represents the attenuation of the primary Au^+ ions due to collisions with electrons and the second term due to the collisions with protons. σ_{ei} and σ_{loss} denote the ionization cross sections by electrons and protons (more generally we should include other heavy articles of ions, too), respectively.

This rate equation (51) has to be integrated over the different path length l according to the ions considered. The path lengths marked with l_0, l_1, l_4, and l_5 in Fig. 24 correspond to that of the in-coming edge region, that in the main plasma before reaching the core plasma part, that of the main plasma after sensing the core part, and that of the out-going edge plasmas, respectively, while the primary Au^+ ions have to pass. The main collisions for the plasma diagnostics of the central plasmas occur over a relatively short path length at the central plasma (δl). Then, the product secondary Au^{2+} ions pass through l_2 and l_3, respectively.

The attenuations of the primary Au^+ ion beam current I_{B1} along l_1 before reaching the core region of the main plasma is given by

$$I_{B1} = I_{B0} \exp\left(- n_e \frac{\left\langle \sigma_{ei}^{1,2} v_e \right\rangle}{v_B} l_1 - n_{H^+} \frac{\left\langle \sigma_{loss}^{1,2} v_B \right\rangle}{v_B} l_1 \right), \tag{52}$$

where I_{B0} is the injected Au^+ ion beam current at the injection port, where their attenuation in the plasma edge region (l_0) is already taken into account. The superscript "1, 2"of σ denotes the charge variation of Au (this case corresponds to the ionization from Au^+ to Au^{2+}). As already pointed out in a previous work [24], the collisions with neutral particles in the edge region and impurity ions in the core region have to be taken into account to obtain more accurate information. Then, the secondary product Au^{2+} ion beam current I_{B2} reaching the plasma exit boundary is given by

$$I_{B2} = \frac{\kappa_{mcp} I_{B1} \delta l}{v_B} \left(n_e \left\langle \sigma_{ei}^{1,2} v_e \right\rangle + n_{H^+} \left\langle \sigma_{loss}^{1,2} v_B \right\rangle \right) \times \exp\left(- n_e \frac{\left\langle \sigma_{ei}^{2,3} v_e \right\rangle}{v_B} l_2 - n_{H^+} \frac{\left\langle \sigma_{loss}^{2,3} v_B \right\rangle}{v_B} l_2 \right), \tag{53}$$

where κ_{mcp} is the detection efficiency of the MCP and δl is the effective observation length in the central plasmas. The first term on the right-hand side represents the secondary ion production at

the core along δl and the second term the ion attenuation along l_2 before reaching the edge plasma region which has also to be corrected for similar ion loss, as mentioned before.

Substituting Eq. (52) into Eq. (53), the ratio $(I_{B2} / I_{B0})_{cal}$ is calculated using the effective observation length δl = 0.6 mm [25], and the beam path lengths l_0 = 3.0, l_1 = 1.2, l_2 = 1.4 and l_3 = 3.0 m, respectively. These path lengths are estimated by the integration over the trajectories of the primary Au^+ and secondary Au^{2+} ion beams. If we have taken into account the plasma ion collision processes, the calculated ratio $(I_{B2} / I_{B0})_{cal}$ decreases significantly and becomes closer to an experimental observation than that with the electron collision process alone. Still the disagreement between calculated and measured signals remains large. For the plasmas with $n_e = 1\times10^{19}$ m^{-3} and T_e = 1.5 keV, and Au^+ ion energies of 1.62 MeV and 5.33 MeV (assuming $\kappa_{mcp} = 0.3$, extrapolated from that of the data sheet), the ratio $\chi \equiv (I_{B2} / I_{B0})_{exp} / (I_{B2} / I_{B0})_{cal}$ were obtained to be 2×10^{-2} for both shots #67418 and #67035. In more recent experiments after a few modifications of the beam transport of the energy analyzer system, we have obtained the ratio χ = 0.1 under shot #76995 with $n_e = 0.5\times10^{19}$ m^{-3} and T_e = 2.0 keV. Still large difference in one order of magnitude would have been due to a number of reasons: 1) the not-established detection efficiencies of the MCP used, 2) the errors of the calculated cross sections and 3) the plasma density profiles along the ion paths. So far we did not have the absolute detection efficiency in a MeV region of heavy ion beam. Soon we are planning to calibrate the MCP by comparing the Au^+ and Au^{2+} ion beam current by a Faraday cup at the exit of the tandem accelerator.

9. Conclusion

The interactions between heavy ion beams and gas targets in the gas cell of the tandem accelerator have been studied to understand the charge changing processes, to optimize the charge fraction for the Au^+ beams, and to improve the availability of the HIBP diagnostics.

In the present model to predict the charge fractions from Au^- to multi-charged Au ions, we have calculated the cross sections for the electron loss and the capture processes with the charge fractions of up to Au^{4+} ions. The electron ionization processes from Au^- to multi-charged positive ions are treated theoretically by the Firsov model. On the other hand, the electron capture processes are calculated using the CAPTURE code. The present analyses based upon these calculated cross sections explain semi-qualitatively the experimental charge fractions at the beam energy of 3 MeV Au^- colliding with neutral Ar gas.

The above collision processes and their cross sections are also included to estimate the beam attenuation in plasmas at LHD. The signal level of the secondary beam is calculated using

the plasma parameters in a core plasma region and the gas densities in a peripheral region of LHD. We found that the heavy ion beam in the core plasma region is significantly attenuated due to the main H^+ ions and the impurity C^{6+} ions in the plasmas. The discrepancy of the signal level for the secondary beam is still one order of magnitude between our estimation and experiment. More careful analysis, i.e. calibration of MCP, and inclusion of core plasma and edge neutral profiles, would be required to establish the high performance diagnostics in addition to the basic function (plasma potential and fluctuation measurements) of the HIBP system.

Acknowledgements

We would like to thank Drs. A. Takagi of KEK and A. Taniike of Kobe University for their advices. The authors would also like to thank Drs. D. Kato and P. Goncharov (NIFS) for valuable discussions. In the beam attenuation calculations, one of authors (M.N.) appreciates Drs. R. K. Janev at Macedonian Academy of Sciences and Arts, M. Kobayashi and M. Shoji at NIFS for discussions. This work is supported in part by JSPS grant #18740357, NIFS06KCBR001, NIFS ULBB505, and NIFS/NINS under the project of Formation of International Network for Scientific Collaborations. One of us (V.P.S) was supported in part by INTAS grant Nr 06-1000012-8530.

References

[1] A. Fujisawa, H. Iguchi, A. Taniike, M. Sasao, and Y. Hamada, IEEE Trans. Plasma Sci. **22**, 395 (1994).

[2] T. Ido, A. Shimizu, M. Nishiura, A. Nishizawa, S. Katoh, T. P. Crowley, K. Tsukada, M. Yokota, H. Ogawa, T. Inoue, Y. Hamada, and the LHD experimental Group, Rev. Sci. Instr. **77,** 10F523 (2006).

[3] M. Nishiura, T. Ido, A. Shimizu, S. Kato, K. Tsukada, A. Nishizawa, Y.Hamada, Y. Matsumoto, A. Mendenilla, and M. Wada, Rev. Sci. Instr. **77,** 03A537 (2006).

[4] J.F. Ziegler, J.P. Biesrsack, and U. Littmark (ed. by J.F. Ziegler): *The Stopping and Range of Ions in Solids* (Pergamon, New York, 1985). Part I, p. 48.

[5] W.D. Wilson, L.G. Haggmark, and J.P. Biersack: Phys. Rev. B **15**, 2458 (1977)

[6] L.D. Landau and E.M. Lifshiz: *Theory of Fields* (Addisson-Wesley, Reading, Massachusetts and Pergamon Press, London, 1971)

[7] O.B. Firsov: Sov. Phys. – JETP **32**, 696 (1957): Sov. Phys. – JETP **34**, 308 (1958): Sov. Phys. – JETP **36**, 1076 (1959)

[8] D.R. Lide (ed.): *Handbook of Chemistry and Physics* 2000–2001, 81st edn (Boca Raton, LA: CRC Press, 2001)

[9] H. Luna, F. Zappa, M.H.P. Martins, S.D. Magalhães, G. Jalbert, L.F.S. Coelho and N.V. de Castro Faria: Phys. Rev. A **63,** 052716 (2001)

[10] A.C.F. Santos and R.D. DuBois: Phys. Rev. A **69,** 042709 (2004)

[11] H. Tsuji, J. Ishikawa, T. Maekawa, and T. Takagi: Nucl. Instr. Meth. B **37/38**, 231 (1989)

[12] V.P. Shevelko, I.Yu. Tolstikhina, and T. Stöhlker: Nucl. Instr. Meth. B **184**, 295 (2001)

[13] V.P. Shevelko, O. Rosmej, H. Tawara, and I.Yu. Tolstikhina: J. Phys. B **37**, 201 (2004)

[14] R.K. Janev, L.P. Presnyakov, and V.P. Shevelko: *Physics of Highly Charged Ions* (Springer Verlag, 1985)

[15] H. Knudsen, H.K Haugen, and P. Hvelplund: Phys. Rev. A **24**, 2287 (1981)

[16] N. Bohr and J. Lindhard: K. Dan. Vidensk. Selsk. Mat. Fys. Medd. 28, no. 7 (1954) (see also D.S.F. Crothers and N.R. Todd: J. Phys. B **13**, 2277 (1980))

[17] H-D. Betz: Rev. Mod. Phys. **44**, 465 (1972)

[18] A. Taniike: *Energy Loss Mechanism of a Gold Ion Beam on a Tandem Acceleration System* (NIFS, Nagoya, PhD Thesis) NIFS Report-352 (1995)

[19] L.A. Vainshtein and V.P. Shevelko: *Atomic Physics for Hot Plasmas* (IOP, Bristol, 1993)

[20] H.M. Hartley and H.R.J. Walters: J. Phys. B **21**, L43 (1988)

[21] Th. Peter and J. Meyer-ter-Vehn: Phys. Rev. A **43**, 2015 (1991)

[22] Y.S. Kim and R.H. Pratt: Phys. Rev. A **27**, 2913 (1987)

[23] M. Nishiura, T. Ido, A. Shimizu, H. Nakano, T. Kato, S. Kato, Y. Hamada, LHD experimental group, V. P. Shevelko, R. K. Janev, and M. Wada, Rev. Sci. Instr. In press.

[24] M. Nishiura, T. Ido, A. Shimizu, R. K. Janev, T. Kato, V. P. Shevelko, S. Kato, K. Tsukada, M. Yokota, H. Ogawa, T. Inoue, H. Nakano, Y. Hamada, and LHD Experimental Group, Plasma and Fusion Research, **2**, S1099 (2007).

[25] T. Ido, A. Shimizu, M. Nishiura, Y. Hamada, S. Kato, A. Nishizawa, and H. Nakano, Plasma and Fusion Research. **2**, S1100 (2007)